



# Human Stem Cell–Derived Cardiomyocytes Integrate Into the Heart of Monkeys With Right Ventricular Pressure Overload

Cell Transplantation  
Volume 33: 1–20  
© The Author(s) 2024  
Article reuse guidelines:  
sagepub.com/journals-permissions  
DOI: 10.1177/09636897241290367  
journals.sagepub.com/home/cll



Jodi Scholz<sup>1</sup>, Frank J. Secreto<sup>2,3</sup>, Joan Wobig<sup>4</sup>, Joe Kurian<sup>5</sup>, Clint Hagen<sup>4</sup>, Alexandra Zinnen<sup>5</sup>, Don Vu<sup>5</sup>, Steven J. Johnson<sup>5</sup>, Frank Cetta<sup>6</sup>, Yasir Qureshi<sup>6</sup> , Rachel Reams<sup>7</sup>, Bryan Cannon<sup>6,8</sup>, Christina M. Heyer<sup>4</sup>, Minhwang Chang<sup>9</sup>, Numrah Fadra<sup>10</sup>, Jennifer Coonen<sup>5</sup>, Heather A. Simmons<sup>5</sup>, Andres Mejia<sup>5</sup>, Jennifer M. Hayes<sup>5</sup>, Puja Basu<sup>5</sup>, Saverio Capuano<sup>5</sup>, Viktoriya Bondarenko<sup>5</sup>, Jeanette M. Metzger<sup>5</sup>, Timothy J. Nelson<sup>2,3,4,6,8</sup>, and Marina E. Emborg<sup>5,11</sup> 

## Abstract

Cardiac ventricular pressure overload affects patients with congenital heart defects and can cause cardiac insufficiency. Grafts of stem cell–derived cardiomyocytes are proposed as a complementary treatment to surgical repair of the cardiac defect, aiming to support ventricular function. Here, we report successful engraftment of human induced pluripotent stem cell–derived cardiac lineage cells into the heart of immunosuppressed rhesus macaques with a novel surgical model of right ventricular pressure overload. The human troponin+ grafts were detected in low-dose ( $2 \times 10^6$  cells/kg) and high-dose ( $10 \times 10^6$  cells/kg) treatment groups up to 12 weeks post-injection. Transplanted cells integrated and progressively matched the organization of the surrounding host myocardium. Ventricular tachycardia occurred in five out of 16 animals receiving cells, with episodes of incessant tachycardia observed in two animals; ventricular tachycardia events resolved within 19 days. Our results demonstrate that grafted cardiomyocytes mature and integrate into the myocardium of nonhuman primates modeling right ventricular pressure overload.

## Keywords

right ventricular pressure overload, stem cells, cardiomyocytes, rhesus, grafts

## Introduction

Single-ventricle congenital heart defects are rare disorders in which one of the cardiac ventricles is severely underdeveloped or the lack of a ventricular septal wall results in a single chamber. They include hypoplastic left heart syndrome, pulmonary atresia, and tricuspid atresia and are all associated with life-threatening pathologies requiring surgical or catheter intervention within the first days of life<sup>1,2</sup>. Right ventricular pressure overload is a common phenomenon in patients with single-ventricle congenital heart defects, particularly defects resulting in a single chambered right ventricle, since the right ventricle is not designed to work against systemic pressures. Despite surgical interventions, nearly all single-ventricle congenital heart

defect patients experience significant morbidity, eventually leading to heart failure<sup>3</sup>. A ventricular assist device may bridge the gap between heart failure and whole cardiac transplant, but it is a temporary solution<sup>4–6</sup>. Moreover, the availability of donor hearts remains extremely limited, a fact compounded by the young age at which most patients will require a cardiac transplant<sup>3,7</sup>.

Stem cell–based therapies complementary to surgical repair are proposed as an innovative solution to support ventricular function and delay or prevent the need for cardiac transplantation in patients with congenital heart defects. Studies in non-human primates (NHPs) modeling cardiac ischemia have demonstrated that human embryonic stem cell (ESC) and allogeneic rhesus macaque (*Macaca mulatta*) induced pluripotent



stem cell (iPSC)-derived cardiomyocytes survive following intramyocardial delivery, re-muscularize scar tissue, and improve heart function, although they are associated with significant arrhythmias such as ventricular tachycardia (VT)<sup>8–13</sup>. However, cardiac grafting conditions after infarction are strikingly different from congenital heart disease. In the ischemic heart, blocked vascularization produces significant regional myocardial loss, and the grafts are intended to replace extensive areas of necrotic and damaged tissue<sup>10,14,15</sup>. In contrast, congenital heart defects that produce ventricular pressure overload cause chronic physiological stress, inducing myofibril disarray and fibrosis, progressively weakening the heart wall, and decreasing cardiac function<sup>1</sup>. Cardiac grafting for ventricular pressure overload is intended to strengthen and support ventricular function after or in conjunction with surgical repair of the cardiac defect. As such, it requires distribution and integration of transplanted cardiomyocytes with host cardiac cells across the myocardium to be effective. However, the lack of a monkey model of right ventricular pressure overload has hampered efforts to evaluate cell transplantation therapies for clinical application. The overarching aim of this study was to assess the feasibility and safety of grafting human iPSC-derived cardiac lineage cells (hiPSC-CLs) in a novel NHP model of functional right ventricular pressure overload, prior to clinical translation.

## Materials and Methods

### Ethics Statement

The present study was performed in strict accordance with the US Animal Welfare Act and Regulations and recommendations in the National Research Council Guide for the Care and Use of Laboratory Animals (8th edition, 2011) in an AAALAC-accredited facility [Wisconsin National Primate Research Center (WNPRC), University of Wisconsin–Madison] with the approval of the IACUC. All

efforts were made to minimize the number of animals utilized and to ameliorate any distress. Human dermal punch biopsies were obtained following documented review and approval from the Institutional Review Board (IRB # 10-006845) at Mayo Clinic, Rochester, MN, USA, and collected following written informed consent by the patient, in accordance with the Declaration of Helsinki.

### Animal Subjects

Adult male and female rhesus macaques (*Macaca mulatta*) were used in this study (Supplementary Table 1). Animals were provided water *ad libitum* and fed a commercial NHP diet (2050 Teklad Global 20% Protein Primate Diet, Harlan Laboratories) twice daily, supplemented with a variety of produce and treats. A nutritional shake (Ensure®, Abbot Laboratories) was administered by oro-gastric gavage during anesthetic recovery for experimental procedures as needed. Animals with decreased appetite were offered soaked chow to encourage eating.

Anesthesia for surgery was induced with ketamine (5–15 mg/kg IM) and midazolam (0.1–0.3 mg/kg IM) followed by propofol (1–5 mg/kg IV) as needed. Animals were maintained on isoflurane delivered by positive pressure ventilation with the use of constant rate infusions of fentanyl (1–10 µg/kg/h IV), ketamine (10–20 µg/kg/h IV), and/or lidocaine (25–50 µg/kg/min IV). Analgesic management included an intercostal nerve block at the planned incision site and at least one space cranial and caudal with liposomal bupivacaine (1 mg/kg IM) and regular bupivacaine (1 mg/kg IM). Intraoperative analgesia also included an incisional block using liposomal bupivacaine at the time of closure (4.4 mg/kg IM). Postoperatively, hydromorphone (0.1 mg/kg IM) was administered every 2–4 h for the first 36–48 h, followed by buprenorphine HCl (0.3 mg/kg IM) every 8–12 h for the subsequent 24 h. Meloxicam (0.2 mg/kg SQ loading dose, 0.1 mg/kg SQ or PO maintenance dose) was administered upon recovery and for at least 5 additional days. During the

<sup>1</sup> Department of Comparative Medicine, Mayo Clinic, Rochester, MN, USA

<sup>2</sup> Department of Medicine, Division of General Internal Medicine, Mayo Clinic, Rochester, MN, USA

<sup>3</sup> Department of Molecular Pharmacology and Experimental Therapeutics, Mayo Clinic, Rochester, MN, USA

<sup>4</sup> Todd and Karen Wanek Family Program for HLHS at Mayo Clinic, Rochester, MN, USA

<sup>5</sup> Wisconsin National Primate Research Center, University of Wisconsin–Madison, Madison, WI, USA

<sup>6</sup> Division of Pediatric Cardiology, Department of Pediatric and Adolescent Medicine, Mayo Clinic, Rochester, MN, USA

<sup>7</sup> StageBio, Mt. Jackson, VA, USA

<sup>8</sup> Cardiovascular Medicine, Mayo Clinic, Rochester, MN, USA

<sup>9</sup> HeartWorks, Rochester, MN, USA

<sup>10</sup> Department of Quantitative Health Sciences, Mayo Clinic, Rochester, MN, USA

<sup>11</sup> Department of Medical Physics, University of Wisconsin–Madison, Madison, WI, USA

Submitted: May 28, 2024. Revised: September 18, 2024. Accepted: September 24, 2024.

### Corresponding Authors:

Timothy J. Nelson, Department of Medicine - General Internal Medicine and Department of Pharmacology and Experimental Therapeutics, Mayo Clinic, Rochester, MN 55905, USA.

Email: nelson.timothy@mayo.edu

Marina E. Emborg, Department of Medical Physics and Wisconsin National Primate Research Center, University of Wisconsin–Madison, Madison, WI 53715, USA.

Email: emborg@primate.wisc.edu

first 72 h post-operatively, animals were intensely monitored for signs of pain or cardiorespiratory complications. Throughout the study, daily observation and documentation of health status were performed, and animals were weighed at least weekly. The immunosuppressed monkeys were monitored for development of diabetes, a known side effect of tacrolimus; three animals (BO4-2, VC4-3, VC12-1) were treated for the condition with glargine insulin.

### **Generation of hiPSCs and Differentiation Into hiPSC-CLs**

Human fibroblast cells were isolated from dermal punch biopsies and reprogrammed into hiPSCs via the Sendai 2.1 kit (Thermo Fisher, cat.# A34546) and assessed for etoposide sensitivity as previously described<sup>16,17</sup>. Three hiPSC clones were expanded and cryopreserved for each reprogrammed fibroblast culture. Approximately  $30 \times 10^6$  hiPSCs ( $12 \times 60$  mm 50% confluent plates) were adapted to suspension culture, expanded to  $\sim 300 \times 10^6$  hiPSCs, and differentiated for 20 days using a Wnt signal modulation-based method similar to a previously described culture system<sup>18</sup>, except substituting a 1:1 mixture of mTeSR1 and StemPro hESC SFM (Invitrogen, A1000701) for mTeSR1 (Stemcell Technologies, 85850) alone. Day 20 hiPSC-CLs were cryopreserved in CryoStor CS10 (Stem Cell Technologies, cat.# 100-1061) at a density of  $10\text{--}40 \times 10^6$  cells/ml and stored in liquid nitrogen. Each hiPSC-CL-differentiated line was assigned a unique lot number; all cells were counted using the Vi-Cell XR cell viability analyzer (Beckman Coulter). Karyotype analyses were performed on a sample of suspension culture hiPSCs collected on the first day (day 0) of cardiac initiation. Day 0 hiPSCs were plated on Geltrex (Thermo Fisher, A1413201) coated 60 mm culture plates and maintained in mTeSR1 feeder-free stem cell maintenance media for 48–96 h prior to delivery to Mayo Clinic Genetics and Genomics Laboratories for G-Band analysis. A minimum of 20 metaphase analyses were conducted per sample. Cells exhibiting  $\geq 2$  genomic changes were labeled “abnormal.” Potential anaerobic and aerobic bacteria contamination was assessed using the Bactec FX40 (BD) automated detection system (14 days incubation at 35°C). Endotoxin levels were determined via the Endosafe nexgen-PTS instrument (Charles River), and Mycoplasma screening on conditioned media ( $\geq 24$  h cell exposure) and cell pellets at the Immunology Core Facility, Mayo Clinic Scottsdale, AZ, using the Lonza MycoAlert™ PLUS Kit (Lonza, LT07-710). All assay samples were collected on the day of cardiomyocyte harvest.

### **hiPSCs and hiPSC-CLs Specific Characterization**

Flow analysis for the surface makers TRA-1-60 (Invitrogen, MA1-023-PE) and TRA-1-81 (BD, 560793) was performed on  $2.5 \times 10^5$  fresh D0 hiPSCs as previously reported<sup>17</sup>. Data were collected (20,000 events per run) using a CytoFLEX

flow cytometer and analyzed for the percentage of cTnT/cTnI protein levels via Kaluza analysis software (Beckman Coulter). Etoposide sensitivity assay analysis was performed on plated iPSCs ( $0.25 \times 10^6$  cells/well) as previously described<sup>17</sup>, with the substitution of Live Dead Near-IR (ThermoFisher, L34975) and APO2.7-PE (Beckman Coulter, IM2088U) for propidium iodide and Annexin-FITC, respectively. EC50 values were calculated using an in-house R-script and based upon dose-response curves generated from eight treatment groups, with averages from each group determined from three technical replicates.

Cytoplasmic flow analysis for cTnT (BD, 564767) and cTnI (BD, 564409) in hiPSC-CLs was performed as previously described<sup>17</sup>. Data collection and analysis used the above-mentioned methods for analyzing TRA-1-60 and TRA-1-81. Cardiomyocyte electrophysiological subtype specification was determined via ArcLight optical sensor analysis on plated D20 iPSC-CL cells<sup>19</sup>. Briefly, APD90 and APD50 values were calculated using an in-house MatLab script from 20 second videos of spontaneously beating cells. The APD90/APD0 ratio was determined from the mean of individual action potentials captured from 30 individual cells.

### **RNA Sequencing**

Total RNA isolated from D0 hiPSCs and D20 hiPSC-CLs was sequenced using Illumina's Novaseq in paired end mode resulting in 101 bp paired end reads. Fastq files for all samples were processed using the Mayo RNA-Seq bioinformatics pipeline, MAP-RSeq 3.1.4 hg<sup>20</sup>. Gene and exon expression quantification was performed using the Subread package to obtain both raw gene counts and normalized Fragments Per Kilobase per Million mapped reads (FPKM) values<sup>21</sup>. Finally, FASTQC and MultiQC tools were used for comprehensive quality control assessment of the aligned reads<sup>22</sup> and a final html report was generated by the MAP-Rseq pipeline. Using the raw gene counts report from MAP-RSeq, differentially expressed genes between D0 iPSC and D20 iPSC-CL cells were assessed using the bioinformatics package edgeR 2.6.2<sup>23</sup> and reported using a magnitude of fold change (log2 scale) and their level of significance (false discovery rate, FDR < 5%).

### **Pulmonary Artery Banding Model**

Pulmonary artery banding (PAB) surgery was adapted from a swine model<sup>24</sup>. A left thoracotomy was performed at approximately the third intercostal space to access the pulmonary artery (PA). The PA was dissected from the aorta, encircled with umbilical tape (1/8" Nonabsorbable Surgical Cotton, Ethicon), and sequentially tightened with ligating clips (Ligacclip® Extra Medium Titanium Clips, Ethicon Endo-Surgery, LLC). Animals P1 and P2 received a saline bolus (30 ml/kg IV) prior to the placement of the PAB. Intraoperative

transthoracic ultrasound was performed to measure the pressure gradient across the band and the degree of tricuspid regurgitation. The tightening of the band was slowly continued by the addition of clips until the systolic mean Doppler pressure gradient approximated 15–23 mmHg, mild to moderate tricuspid regurgitation was present, and the systemic blood pressure remained stable to mildly decreased. The air in the pleural cavity was mechanically evacuated and then a chest tube was placed under a water seal. The incision was closed using standard closure technique, with the chest tube removed during closure. Throughout surgery, heart rate, direct blood pressure, respiratory rate, temperature, and electrocardiography were continuously monitored.

### *Intramyocardial Delivery of hiPSC-CLs or Vehicle*

Two weeks after PAB surgery, intramyocardial injections of hiPSC-CLs or vehicle (Cryostor10, Biolife Solutions) were performed<sup>24,25</sup>. All animals were immunosuppressed with a combination of abatacept, tacrolimus, and methylprednisolone. Tacrolimus dosing (0.03 mg/kg IM twice daily) began 5 days before injection surgery (or before day 0 for banding only animals). Methylprednisolone (30 mg/kg IV bolus) was administered the day prior to surgery followed by a tapered dose (6 mg/kg IM once daily for 2 days) and then a maintenance dose (3 mg/kg IM once daily) until necropsy. Abatacept (12.5 mg/kg SQ) was initiated the day prior to surgery and redosed every 2 weeks. Levels of tacrolimus were measured at least weekly and dosing adjustments were made as needed to maintain a therapeutic blood concentration between 5 and 15 ng/ml (Supplementary Table 2).

The products to be injected were transported to the surgical facility in a liquid nitrogen dry shipper container. For the pilot study, a single lot of cells was used ( $3.5 \times 10^7$  cells/ml). For the definitive study, three separate cell lots were used to produce low ( $7 \times 10^6$  to  $1.1 \times 10^7$  cells/ml) and high ( $3.3$ – $4.7 \times 10^7$  cells/ml) hiPSC-CL doses; surgeons were blind to the vials' contents. After the selected product was manually thawed and gently mixed, it was loaded into 1-ml syringes with a blunt 16-gauge needle. Then, the needle was replaced with a winged infusion set (27-gauge  $\times$   $\frac{1}{2}$  inch, 8-inch tubing, Surfco®, Terumo Medical Corporation). A right thoracotomy at the fourth or fifth intercostal space was performed to access the right ventricle, and the pericardium was incised and retracted to expose the epicardial surface. A 2- to 4-cm target injection area focused on the mid-right ventricle was visually identified. Avoiding the coronary vessels and the conduction system, the needle was inserted into the myocardium and 0.2 ml of product was delivered over 10 s. The needle was held in place for an additional 20 s to prevent leakage and slowly removed. The injection procedure was repeated in the target area to deliver  $2 \times 10^6$  or  $10 \times 10^6$  cells/kg for the low-dose and high-dose hiPSC-CL groups, respectively (Supplementary Table 1). Product

was delivered within 20 min from the start of thawing time. Surgeries were all performed at the same surgical site by the same surgeon.

### *Telemetry Device Implantation and Continuous Cardiac Monitoring*

At the conclusion of the PAB surgery, an implantable cardiac monitor (Reveal LINQ, Medtronic, Minneapolis, MN) was inserted into the subcutaneous space on the left thorax. After proper placement was verified by an adequate P wave and QRS detection, the skin was closed. The device was programmed to detect tachycardic events ( $\geq 222$  bpm) lasting longer than 16 beats, bradycardic events ( $\leq 30$  bpm) lasting longer than 4 beats, and pause events lasting longer than 3 s. The implantable cardiac monitor was interrogated with a handheld telemetry wand (Medtronic Patient Connector, Model 24967) connected to the Medtronic CareLink app on a dedicated iPad (Apple iPad Air 2, Model A1566) and directly uploaded into CareLink. Uploaded events were interpreted by a pediatric electrophysiologist blind to the animal's condition to verify the presence of arrhythmias versus sinus tachycardia or artifact.

### *Echocardiography*

Transthoracic echocardiography was performed prior to and immediately after PAB surgery, prior to product injection (day 0 for banding only animals), and every 2–4 weeks until necropsy. For imaging, the animals were anesthetized with ketamine (5–10 mg/kg IM), or as described above for surgery days. If tachycardia was identified, animals were originally anesthetized with alfaxalone (2–10 mg/kg IM), but it was transitioned to ketamine (5–10 mg/kg IM) and midazolam (0.2 mg/kg IM) for deeper sedation. The animals were imaged in left lateral decubitus or supine position with a Vivid-q (GE Health Care Systems) echocardiographic platform using 4 and 6 MHz probes (GE 6S and GE M4S, GE Health Care Systems). Offline post-processing, including measurement of ventricular function, was performed using an EchoPac (GE) system. Imaging was performed from subcostal, parasternal, and apical acoustic windows. Biventricular systolic function was assessed with 2D and M-mode imaging. The systolic mean and maximum instantaneous gradients across the PAB and the tricuspid regurgitation maximum velocity (when available) were obtained with continuous wave (CW) Doppler interrogation to estimate right ventricular systolic pressure. From the apical view, right ventricular diastolic and systolic areas were measured to calculate fractional area change for assessment of right ventricle systolic function. M-mode imaging to assess TAPSE (tricuspid annular plane systolic excursion) and visual estimates of right ventricle systolic function were also performed.

### Blood Measures

Cardiac markers were evaluated prior to PAB and product injection (or day 0 for banding only animals), and at weeks 2, 4, 8, and 12. Creatine kinase-MB and B-type natriuretic peptide testing in EDTA whole blood or plasma used a fluorescent immunoassay Triage MeterPro (Quidel), while lactate dehydrogenase (LDH) was measured spectrophotometrically in serum using a Vet Axcel (Alfa Wassermann) at WNPRC Clinical Pathology Laboratory (Madison, WI). Troponin I in heparinized plasma was evaluated by chemiluminescent immunoassay with a Centaur (Siemens) or Architect i2000 (Abbott) at Unity Point-Meriter Laboratories (Madison, WI). Tacrolimus levels were measured by immunoassay at the Immunology Center CORE lab of the University of Wisconsin Hospital (Madison, WI).

### Necropsy and Tissue Evaluation

At experimental endpoints, the animals were anesthetized with ketamine hydrochloride (10–15 mg/kg IM) followed by pentobarbital sodium (minimum of 25 mg/kg IV), evaluated for pericardial, pleural, and/or abdominal effusion, and perfused through the left atrium with heparinized saline, followed by 4% paraformaldehyde. A full necropsy of all animals was performed by an ACVP board-certified veterinary pathologist.

After collection, whole hearts were cut with the aid of a calibrated polymethyl methacrylate slice apparatus into 4-mm sections in a transverse plane creating 8 to 12 levels from the base to the apex<sup>26,27</sup>. The tissue was post-fixed for 24 h in 4% paraformaldehyde, transferred to 70% ethanol, and processed for paraffin embedding. Blocks of embedded tissue were cut on a standard rotary microtome in 5- $\mu$ m sections and mounted on positively charged slides. From each block, eight H&E- and two Masson's trichrome-stained slides were prepared and evaluated. Grading for myofiber disarray, fibrosis, and cytologic alteration was based on an estimated percentage of heart chamber myocardial area affected: ~3%–5%, minimal; ~6%–15%, mild; ~16%–25%, moderate; ~26%–35%, marked; and >36%, severe. Grading for myofiber disarray and/or myocardial fibrosis in the ventricles reflected the most pronounced level(s) of the heart affected. Grading and assessment of fibrosis was based on Masson's trichrome, with reference to H&E-stained slides.

H&E-stained tissue sections of each organ were evaluated and reviewed by ACVP board-certified veterinary pathologists. Tissues evaluated included heart, aorta, bone marrow, bone, brain, epididymis, esophagus, eye, gallbladder, adrenal gland, pituitary gland, salivary gland, seminal vesicle, thyroid gland, kidney, distal colon, liver, lung, tracheobronchial lymph node, skeletal muscle, sciatic nerve, ovary, pancreas, skin, jejunum, cervical spinal cord, spleen, stomach, testes, thymus (if present), tongue, trachea, and urinary bladder. Histological findings were analyzed and recorded; they were

related to immunosuppression, surgical manipulation, and/or pathologies consistent with background findings within monkeys at the WNPRC colony.

### Immunohistochemistry, Imaging, and Graft Size Assessment

Cardiac sections were immunostained with the following primary antibodies: human cTnI (Abcam AB52862), cTnT (Invitrogen MA512960), Ki-67 (Thermo Fisher Scientific 14569882), CD31 (R&D Systems AF3628), connexin 43 (Invitrogen 13-8300), CD45 (DAKO M0701), CD68 (Sigma HPA048982), and/or desmin (NSJ Bioreagents V3200) and counterstained with hematoxylin (VWR, Radnor, PA), with the exception of immunofluorescence staining, as previously described<sup>26–28</sup>. Positive and negative controls were processed in parallel. Positive controls included human cardiac tissue (human cTnI) and rhesus spleen (immune markers). Negative controls omitted primary antibodies.

The presence of human cTnI+ grafts was assessed across all cardiac levels in human cTnI immunostained sections counterstained with hematoxylin. Using a Zeiss Axioimager M2 microscope equipped with a Qimaging camera, one tissue section per cardiac level was blindly evaluated at 2.5 $\times$  magnification. When human cTnI+ cells were observed, the cardiac level and location were recorded, and an image was captured. The size of the area of engraftment per cardiac level was measured using NIH ImageJ software percent area above threshold (%AAT) function. Within each 2.5 $\times$  image, all human cTnI-immunoreactivity was manually outlined to define a region of interest (ROI), and %AAT was measured in the ROI. The %AAT was then multiplied by the ROI area to determine the size (mm<sup>2</sup>) of the human cTnI+ area within that image. Human cTnI+ area was summed across all images per level for total graft area per level, and then summed across all levels to obtain the total grafted area per subject. To calculate the graft size as a percentage of the right ventricle area, the total right ventricle area was obtained by drawing ROIs in ImageJ around the right ventricle tissue at each cardiac level and summing across all levels. The total grafted area per subject was then divided by the total right ventricle area for the subject and multiplied by 100.

Graft heterogeneity between and within treatment groups was illustrated with representative images of relatively low, medium, and high graft interdigitation or core maturity/organization. Interdigitation level was assigned by the degree of “blending” between the human cTnI+ cells and rhesus cardiac cells at the edge of each graft (low = graft clearly demarcated; high = edge of the graft has regular interdigitation/intermix of human cTnI+ and cTnI- cells). Graft maturity/organization level was based on the morphology of the human cTnI+ cells at the approximate center of the graft [low = graft core with irregular/pleomorphic cell morphology and alignment; high = graft core featuring cells with

“spindle-like” morphology and more parallel cell alignment]. Desmin expression was quantified in a subgroup of animals using immunofluorescent images collected via 10× XY stitching to include the entire cTnI+ grafted area. Image brightness was adjusted using identical Lookup Tables (LUTs) settings across images, and the desmin channel image was exported as a black and white tif. Using ImageJ, the tif color was inverted, an ROI was drawn around the grafted area, and the percentage of the area above threshold (%AAT) was calculated using a predetermined threshold to detect desmin-immunoreactivity.

Immunofluorescence imaging was performed using a Nikon AIR confocal microscope with 405, 488, 561, and 640 wavelength lasers using NIS Elements version 5.20.02. Detectors for the 488 and 561 lasers were high-sensitivity GaAsP PMTs; detectors for 405 and 640 lasers were HS PMTs. Brightfield imaging was performed on either an Olympus BX43F microscope with a DP23 camera and cellSens Standard 4.1.1 software or a Nikon Eclipse Ti2 microscope with a DS-Ri2 camera and NIS Elements software. During the preparation of images for figures, any adjustments made to images, such as adjusting of brightness or LUTs of immunofluorescence images, were applied to the entire image.

### Statistical Analysis

Data collection and analysis were performed by investigators blind to the treatment groups. Statistical analysis was performed using GraphPad Prism (version 10.0, GraphPad Software). Total graft size was compared between low-dose and high-dose animals using the Mann–Whitney test. The relationship between total cell number injected and total graft size was evaluated using the Pearson correlation coefficient. A *P* value <0.05 was accepted as significant.

## Results

### Generation of hiPSCs and hiPSC-CLs

We generated four hiPSC clones from primary dermal fibroblast cultures originating from three human donors to be used for cardiac grafting. The hiPSCs expressed high levels of TRA-1-60 and TRA-1-81 surface proteins (Supplementary Fig. 1a–d), and their response to etoposide (Supplementary Fig. 1e–h) and RNA profiles were consistent with undifferentiated pluripotent stem cells (Supplementary Fig. 2). The clones were subsequently differentiated into four corresponding hiPSC-CL lots, with detectable levels of cardiac troponin (cTnT/cTnI) expression varying between 57% and 88% (Supplementary Fig. 1i–l). At day 20, hiPSC-CLs exhibited RNA expression profiles typical of pluripotent cell-derived cardiomyocytes (Supplementary Fig. 2). Determination of cardiac chamber specificity of the iPSC-CLs (D20 + 5 days plated) was achieved using a stably transduced ArcLight Ca<sup>+</sup> channel optical sensor. ArcLight-expressing cells exhibit a

rapid change in fluorescence upon depolarization of the ultra-rapid rectifier potassium current ( $I_{Kur}$ ), which can be captured via high-speed digital videography (Supplementary Fig. 3). Analysis of 30 spontaneously beating cardiomyocytes per lot revealed that all four hiPSC-CL lots had action potential profiles consistent with a mixture of typical atrial and ventricular electrophysiological subtypes (Supplementary Fig. 1m–p).

### Methods Development: Creation of a NHP Model of Right Ventricular Pressure Overload and Intramyocardial Cell Delivery Approach

To assess the feasibility of engraftment of hiPSC-CLs in hearts experiencing right ventricular pressure overload, we developed a novel rhesus macaque model based on a swine PAB model<sup>24</sup>. Our primary goals in developing this novel NHP model were to (1) recapitulate the right ventricular pressure overload that occurs in single-ventricle patients who have undergone surgical palliative surgeries and (2) induce a condition that is severe enough to result in histopathology similar to what occurs in these patients, yet survivable for long-term evaluation of cell engraftment. Permanent PAB was initially performed in eight monkeys to induce a pressure gradient across the constriction (Fig. 1A–C; Supplementary Fig. 4a). Animals also received implantable cardiac monitors at the time of PAB surgery. In the first two subjects of this pilot phase (P1, P2), the post-banding systolic mean Doppler pressure gradients across the PAB measured by echocardiography in the immediate post-operative period were 29 and 27 mmHg, respectively; these two subjects received a saline bolus before banding. Both animals expired within 3 days of surgery due to cardiovascular insufficiency; thus, the surgical procedure was adjusted to eliminate the fluid bolus and decrease the pressure gradient. Guided by intraoperative cardiac ultrasound, the remaining animals had a resultant target systolic mean Doppler pressure gradient of 15–23 mmHg (Fig. 1D; Supplementary Fig. 4b) and mild-moderate tricuspid regurgitation (Fig. 1E). A third subject (P3) died intraoperatively during the PAB procedure due to a PA injury. The three subjects (P1, P2, and P3) were not included in the analyses or representative images.

As part of this method development phase, four of the six rhesus with successful PAB were immunosuppressed with a combination of abatacept, tacrolimus, and methylprednisolone. These animals subsequently underwent a second thoracotomy to inject hiPSC-CLs ( $10 \times 10^6$  cells/kg) into the right ventricular myocardium (Supplementary Fig. 4c). Depending on body weight, the total volume injected ranged between 1.4 and 3 ml, administered via 7–15 injections of 0.2 ml each in a 2–4 cm<sup>2</sup> area. Cardiac rhythm monitoring detected arrhythmia events in the two monkeys that underwent banding only: two VT events in animal P4 on day 40 post-PAB and one pause event in animal P5 on day 13 post-PAB. No arrhythmia events

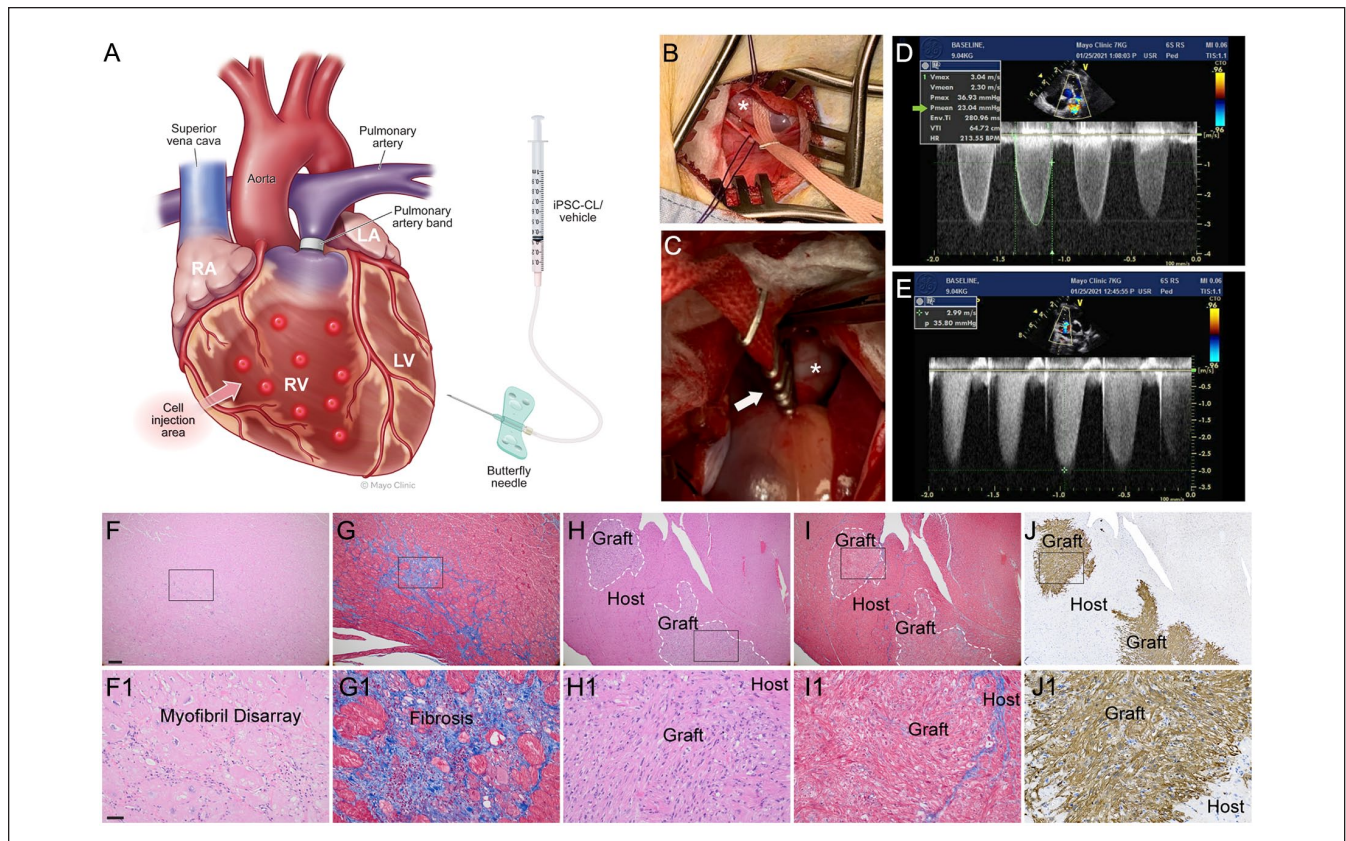


**Figure 1.** Development and characterization of a nonhuman primate model of cardiac pressure overload. (A) Cartoon of cardiac anatomy and surgical targets. (B, C) To create right ventricular pressure overload, a left thoracotomy was performed to access the pulmonary artery (asterisk), which was encircled with umbilical tape and gradually tightened with ligating clips (white arrow). Intraoperative echocardiography was used to measure the pressure gradient across the band as it was tightened by the addition of clips until (D) the gradient reached  $\sim 15$ – $23$  mmHg (green arrow) and (E) mild-moderate tricuspid regurgitation was present. Postmortem analyses detected myofibril disarray (F, F1) (H&E staining) and (G, G1) fibrosis (Masson's trichrome staining, blue coloration) (P5). Grafts of hiPSC-CLs (area demarcated by white dashed line) were recognized with (H, H1) H&E staining and (I, I1) Masson's trichrome staining and confirmed by (J, J1) human cardiac troponin I (cTnI) immunostaining counterstained with hematoxylin (P7). (F1–J1) high magnification images of areas demarcated by black rectangles in (F–J). Scale bar: (F–J)  $200\ \mu\text{m}$ , (F1–J1)  $50\ \mu\text{m}$ .

were detected in the pilot animals receiving hiPSC-CLs (Supplementary Fig. 4c). Postmortem evaluation 4 or 8 weeks after cell delivery (or equivalent timepoints for banding only animals) identified myocardial fibrosis within the right ventricular myocardium with hematoxylin and eosin (H&E) (Fig. 1F), clearly visualized as blue cytoplasmic staining with Masson's trichrome (Fig. 1G). Myofibril disarray was also present and was characterized by variably sized myofibers, enlarged and/or hyperchromatic myofiber nuclei, and occasionally non-aligned and/or branching myofibers (Fig. 1F, G). Last, in the four cell-injected monkeys, the hiPSC-CL grafts were identified in the target region of the right ventricular myocardium as areas of cytological alterations in H&E and Masson's trichrome stainings (Fig. 1H, I), which were positive for human-specific cardiac troponin I (cTnI) immunostaining (Fig. 1J).

### Clinical Safety Assessment of Cardiac Grafts

Based on the methods development study, we performed PAB surgery and placed implantable cardiac monitors in 29 adult rhesus. One female died 8 days after PAB due to acute right ventricular heart failure and was not enrolled in the study. Two weeks post PAB surgery, all 28 surviving animals (14 males and 14 females) with a mean gradient across the PAB greater than  $10$  mmHg were randomly assigned to remain untreated (banding only, BO;  $n = 4$ ) or to receive vehicle (VC;  $n = 8$ ), a low dose ( $2 \times 10^6$  cells/kg, LD;  $n = 8$ ), or a high dose ( $10 \times 10^6$  cells/kg, HD;  $n = 8$ ) of hiPSC-CLs and to be euthanized at 4 or 12 weeks post-intramyocardial injections (Fig. 2A; Supplementary Table 1). Surgeons were blind to the contents of the treatment vials. All animals were immunosuppressed throughout the duration of the study with the same regimen used in the pilot project.

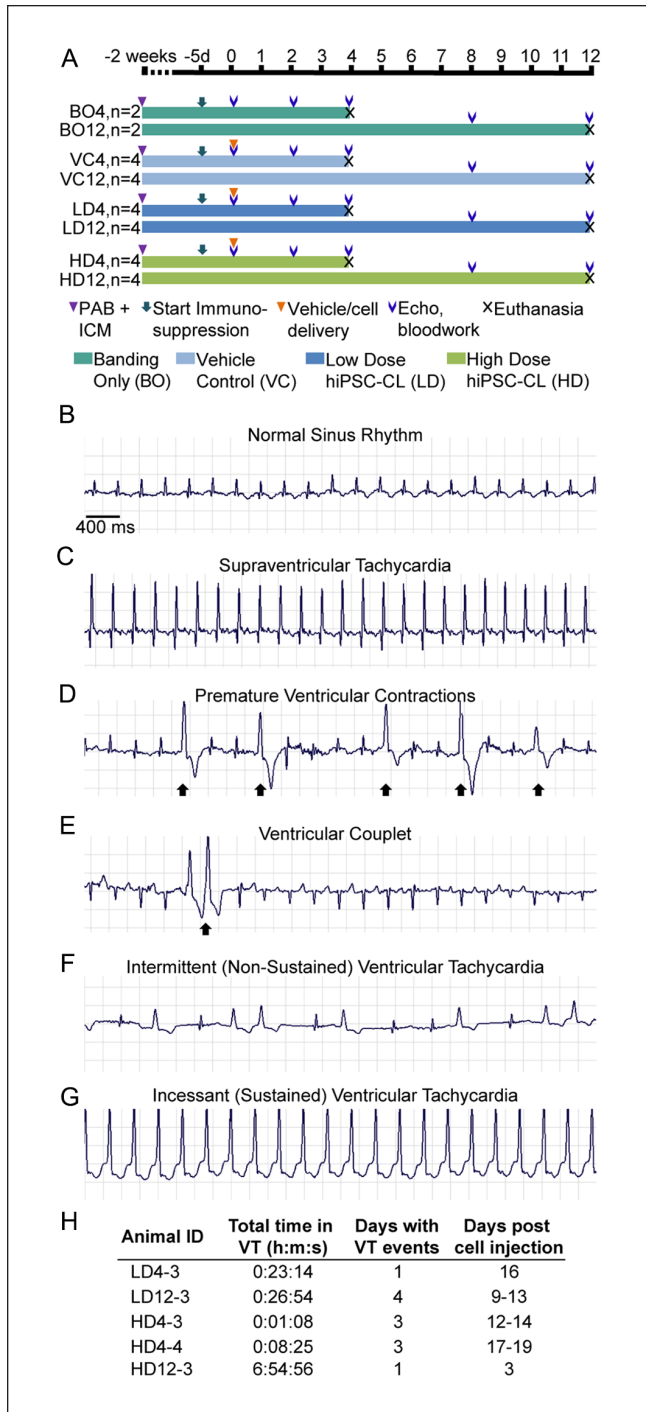


**Figure 2.** Ventricular arrhythmia events detected after injection of hiPSC-CLs. (A) Experimental design evaluating cardiac effects of hiPSC-CLs in 28 monkeys. Representative electrocardiogram (ECG) tracings: (B) normal sinus rhythm, (C) supraventricular tachycardia, (D) premature ventricular contractions (black arrows), (E) ventricular couplet (black arrow), (F) intermittent, non-sustained ventricular tachycardia (VT), and (G) incessant VT. (H) Frequency and duration of all VT events in the five affected subjects. PAB, pulmonary artery banding; ICM, implantable cardiac monitor.

PAB resulted in increases in gradient across the banded area and right ventricular systolic pressure. There were no changes in right ventricular fractional area change or TAPSE (Supplementary Table 3). One animal (HD12-1) was noted to have concentric hypertrophy of the left ventricular walls at the pre-PAB echocardiogram, the degree of which did not change throughout the study. Continuous cardiac rhythm monitoring identified episodes of VT in five of the 16 grafted monkeys (Fig. 2B–G; Supplementary Table 1). One animal in the 12-week hiPSC-CL high-dose group (HD12-3) died 3 days after cell delivery due to incessant VT. One animal in the 12-week low-dose hiPSC-CL group (LD12-3) developed incessant VT 9 days after cell injection and was successfully treated with amiodarone through study endpoint. The other three animals that developed episodic VT events (LD4-3, HD4-3, and HD4-4) were asymptomatic and successfully completed the study without treatment. In these animals, VT resolved within 19 days post cell injection. Other cardiac activity events detected included supraventricular tachycardia, premature ventricular contractions, and ventricular couplets (Fig. 2C–E), which resolved by 28 days (Supplementary Table 1). No significant differences in cardiac events were detected between low- and high-dose groups or between cell lots. None of the animals in the banding only or vehicle groups developed VT (Supplementary Table 1). None of the animals had evidence of dysfunction as measured by echocardiogram and clinical health assessments throughout the study. Outside of the reported arrhythmias, no negative impact on heart health related to the cell transplantation procedures was detected.

Blood was collected at multiple timepoints for hematology and cardiac injury markers. At 2 and 4 weeks post-cell delivery, hematology alterations were consistent with stress; these values returned to at or near baseline levels by weeks 8 and 12 (Supplementary Tables 4 and 5). The cardiac biomarkers creatine kinase-MB and B-type natriuretic peptide were at or near the lower limit of detection in all animals and timepoints. Levels of LDH were measurable with some increases detected, but changes were considered not cardiac specific due to model-related tissue injury. cTnI levels were unremarkable, although some individual animals had minimal increases from baseline levels, most often at weeks 2 and 4.

### Histological Evidence of Graft Distribution Across the Right Ventricular Myocardium

Evaluation of serial whole cardiac sections stained with H&E and Masson's trichrome identified pathological changes associated with increased right ventricular pressure in all animals. Myocardial fibrosis and myofibril disarray were present in the right ventricle (Fig. 1F, G; Supplementary Fig. 5), resembling model development phase findings. In most animals, the severity of these histopathological findings ranged from minimal to moderate, with two vehicle (VC4-3,



VC4-4) and two low-dose 4-week (LD4-3, LD4-4) monkeys displaying marked to severe myofibril disarray and loss, as well as fibrosis. The animal with incessant VT that expired 3 days post-cell injection (HD12-3) had marked myocardial fibrosis and myofibril disarray in the right ventricular myocardium that extended into the interventricular septum, along with mild mononuclear infiltration and areas of mild, multifocal cardiomyocyte necrosis. There were no pathological changes in the left ventricles or left atria of animals in the four study groups (cell-treated or controls) that were definitively different than typical background findings in 4 to 9 years old rhesus macaques at the WNPRC colony. The peripheral regions of the cardiac grafts in all monkeys had minimal multifocal mononuclear cell infiltration or very minimal disorganized incipient fibrosis (Supplementary Fig. 5a, b). Although there was increased connective tissue visible at 4 weeks in the Masson's trichrome-stained cardiac sections (Supplementary Fig. 5b), there was no visible evidence of organized collagen, further extracellular matrix deposition, or encapsulation of the graft by fibrotic tissue at 12 weeks (Supplementary Fig. 5d). Five of the eight low-dose and all eight high-dose monkeys injected with hiPSC-CLs had grafts that, like the pilot animals, were detected as areas of cytological alteration by H&E and were confirmed to be human cTnI+ engrafted cardiomyocytes (Fig. 3A, B).

Human cTnI+ cardiac grafts were mapped across serial tissue sections from cardiac base to apex. Overall, grafts were preferentially located at the mid-section of the heart (Fig. 3C). The sum of human cTnI+ areas per level was used to create a heatmap of the graft distribution per subject. Individual variations were detected between subjects and groups (e.g., lack of grafts in three low-dose subjects). The total graft area per animal (sum of human cTnI+ area in all levels) was used to calculate the mean area per treatment group. The average graft area for low-dose animals (excluding the three subjects without grafts) was  $2.51 \pm 1.34 \text{ mm}^2$  (mean  $\pm$  SD) at 4 weeks ( $n = 3$ ) and  $1.48 \pm 0.03 \text{ mm}^2$  at 12 weeks ( $n = 2$ ), while, in the high-dose animals, graft area was  $2.61 \pm 2.34 \text{ mm}^2$  at 4 weeks ( $n = 4$ ) and  $14.59 \pm 12.17 \text{ mm}^2$  ( $n = 3$ ) at 12 weeks after surgery. The graft size as a percentage of the right ventricle area in low-dose animals was  $0.37\% \pm 0.11$  at 4 weeks and  $0.20\% \pm 0.02$  at 12 weeks, and in high-dose animals was  $0.32\% \pm 0.32$  at 4 weeks and  $1.4\% \pm 1.01$  at 12 weeks (Supplementary Table 6). Due to individual variability, no statistically significant differences were detected between cell dose groups or timepoints. One subject in the 12-week high-dose group (HD12-1) presented the largest graft area over the greatest number of cardiac levels, despite the injection volume and number being adjusted based on body weight. In animals with grafts, a statistically significant correlation was observed between the total number of cells injected and the total graft size per animal ( $P = 0.039$ ), which remained significant when HD12-1 was excluded from analysis ( $P = 0.045$ ) (Supplementary Fig. 6).

### ***Integration, Maturity, and Organization of the Engrafted Human Cardiomyocytes***

The characteristics of the grafts and their integration into the surrounding host tissue varied between subjects at different timepoints. At 4 weeks post-transplantation, cardiac graft foci were clearly demarcated within the host myocardium on H&E staining (Supplementary Fig. 5a, b). The grafted cells were characterized by spindle or pleomorphic morphology with scant, amphophilic cytoplasm (Supplementary Fig. 5a, b; arrows). In comparison, at 12 weeks grafted cells displayed more spindle-like morphology and eosinophilic cytoplasm, often with visible cross-striations characteristic of cardiomyocytes (Supplementary Fig. 5c; arrowheads). Masson's trichrome-stained tissue sections showed variable red staining of the cytoplasm in grafted cells (similar to host cardiomyocytes) at both timepoints, which was more uniform and blended into and between adjacent host cardiomyocytes at 12 weeks (Supplementary Fig. 5d). Human cTnI immunostaining further showcased integration of the graft with the host myocardium, characterized by interdigitation of host and graft cardiomyocytes at the graft perimeter (Supplementary Fig. 7). Grafted cell foci often displayed a mature cardiomyocyte phenotype and frequently organized in a pattern that matched the surrounding host myocardium. Graft core maturity and organization was greater after 12 weeks but was also observed in some grafts at 4 weeks (Supplementary Fig. 8).

Double-label immunofluorescence with antibodies against human cTnI and the non-species-specific cardiomyocyte marker cTnT confirmed these findings (Fig. 4; Supplementary Fig. 9). The organization at the core of the human cTnI+ graft increased over time, from a semi-disordered distribution of cells at 4 weeks to a more parallel pattern matching the configuration of the cTnT+ host tissue at 12 weeks. Expression of the intermediate filament protein desmin, considered a marker of cardiomyocyte maturity, was rarely observed in grafted cells 4 weeks post-transplantation (Fig. 5; Supplementary Fig. 10). By 12 weeks, desmin was abundantly expressed in grafted cells, often present in sarcomeric striation-like patterns, like cTnI (Fig. 5; Supplementary Fig. 10; Supplementary Table 7). Immunostaining against the gap junction protein connexin 43 identified apparent areas of interaction between grafted human iPSC-CLs and host myocardium, which were more common at 12 weeks (Fig. 6A, B; Supplementary Fig. 11). Notably, the endothelial cell marker CD31+ identified blood vessels within the human cTnI+ graft and host tissue (Fig. 7A, B; Supplementary Fig. 12a, b).

### ***Histological Evaluation of Graft Safety and Host Immune Response***

As grafting of hiPSC-derived cardiomyocytes has the potential to generate teratomas<sup>29</sup>, the heart and standardized

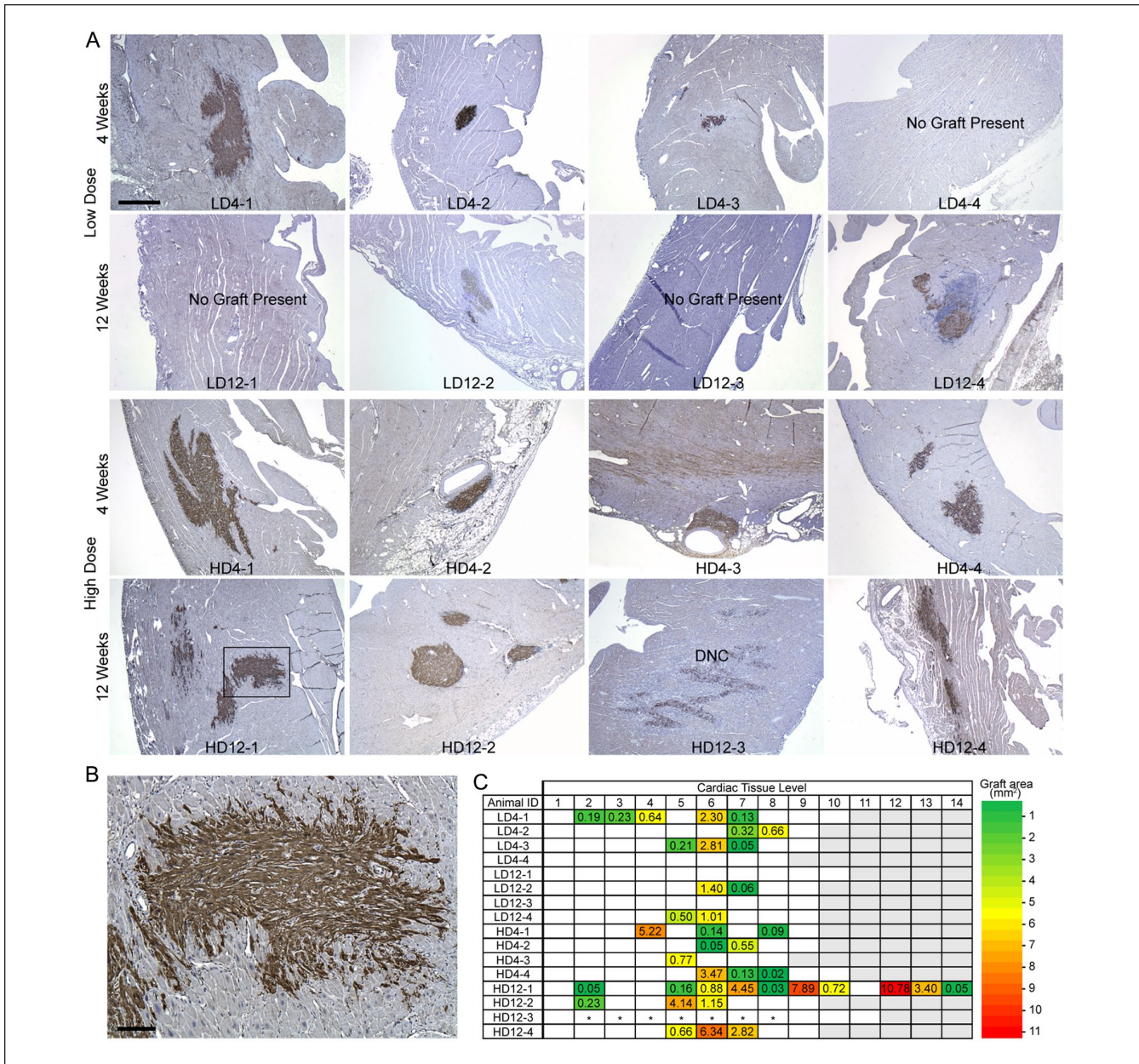


**Figure 3.** Grafts of human cardiac troponin I (cTnI)+ hiPSC-CLs across the right ventricular myocardium. (A) Representative images of the right ventricular myocardium of all hiPSC-CL injected animals. Cardiac tissue was immunostained for human cTnI (brown) and counterstained with hematoxylin (blue). (B) High-magnification image of area demarcated by black rectangle in HD12-1. Scale bar: (A) 1,000  $\mu$ m, (B) 100  $\mu$ m. (C) Heat map of human cTnI+ graft area (mm<sup>2</sup>) per subject across cardiac tissue levels. Each heart was sliced in 4-mm blocks from the apex to the base, and tissue from each block was immunolabeled for human cTnI to detect grafted cells across the entire right ventricle. The number of blocks depended on individual animal size; gray boxes indicate no right ventricle tissue at this level. White, empty boxes indicate no human cTnI+ graft detected. \*, some human cTnI was detected, but graft size was not quantified due to lack of perfusion impacting immunolabeling. DNC, did not complete study.

sentinel tissues were evaluated by board-certified veterinary pathologists. No evidence of teratomas, cellular atypia, or neoplastic cells was identified by macroscopic or light microscopic evaluations. Mitotic figures were not prominent in sections of right ventricular myocardium stained with H&E. The expression of the nuclear protein Ki67 revealed a

small number of proliferating cells per field of view within the human cTnI+ graft and in the surrounding right ventricular myocardium (Fig. 7C, D; Supplementary Fig. 12c, d; Supplementary Table 8).

Some mononuclear cells were observed surrounding the hiPSC-CL xenografts at both 4 and 12 weeks post grafting.

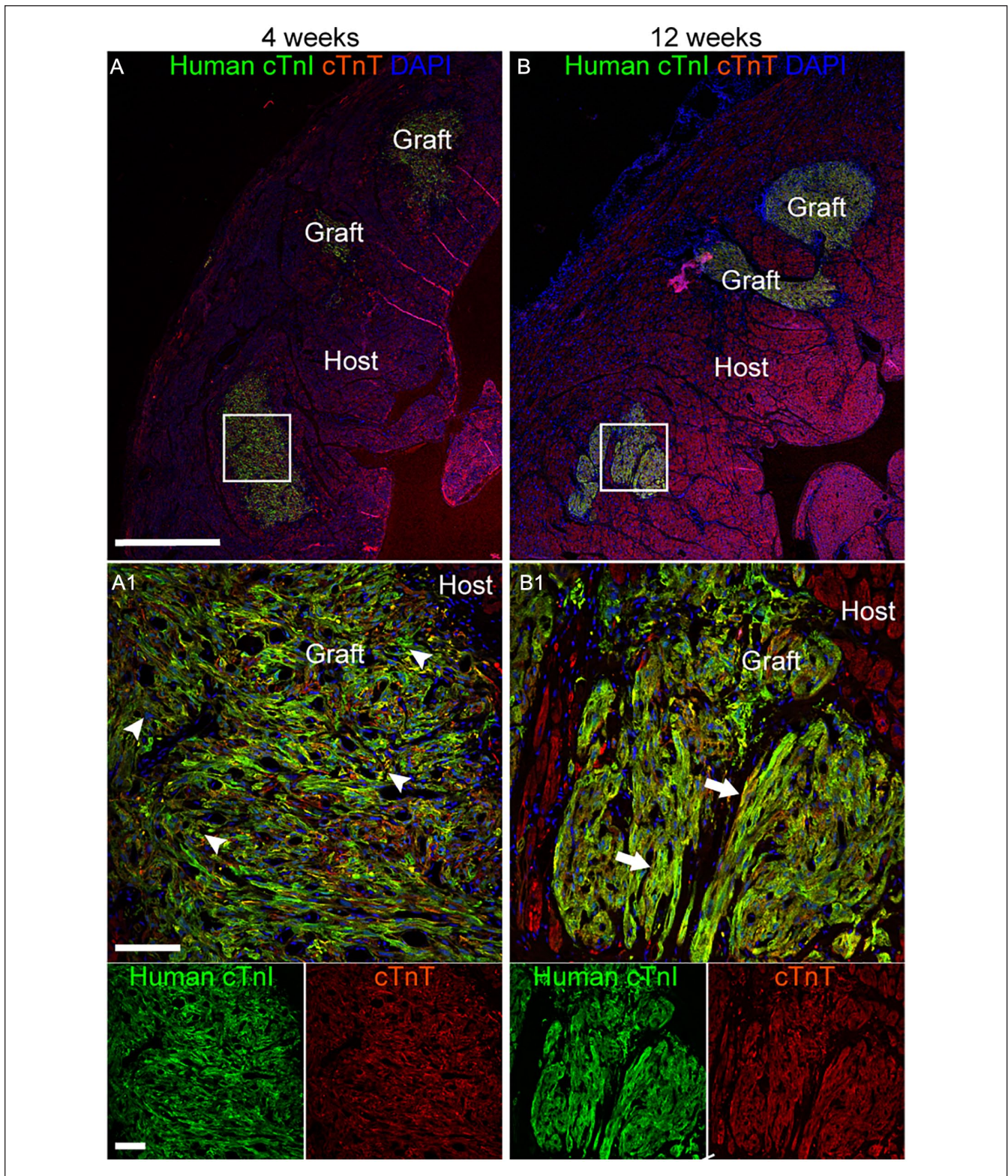


**Figure 4.** hiPSC-CLs integrate into the right ventricular myocardium. (A, B) Representative images from high-dose 4-week (A, HD4-4) and high-dose 12-week (B, HD12-2) subjects showing immunofluorescence labeling of human cardiac troponin I (cTnI) (green) grafted cells integrating into the myocardium (red = rhesus and human cardiac troponin T (cTnT)) counterstained with the nuclear marker 4',6-diamidino-2-phenylindole (DAPI; blue). Grafted cells exhibited increased organization and maturity from 4 (arrowheads—disorganized with pleomorphic morphology) to 12 (arrows—increased parallel organization of cells, spindle-like morphology, and visible cross-striations) weeks. (A1, B1) Higher magnification image of area demarcated by white squares in (A, B). Scale bar: (A, B) 1,000  $\mu$ m, (A1, B1) 100  $\mu$ m.

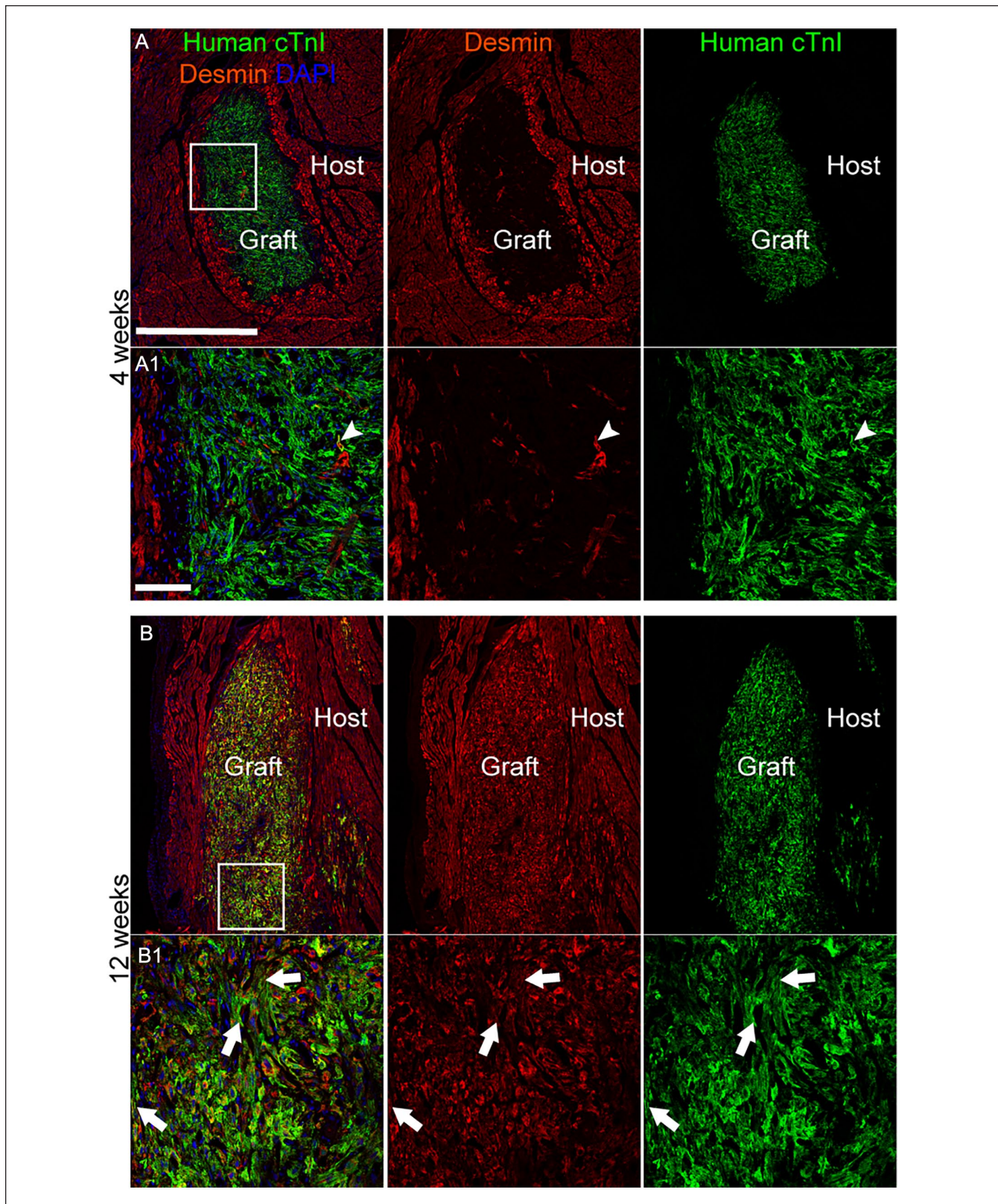


**Figure 5.** Desmin is abundantly present in grafted hiPSC-CLs at 12 weeks post-transplantation. (A, B) Representative images from high-dose 4-week (HD4-1) and high-dose 12-week (HD12-4) subjects showing immunofluorescence labeling of human cardiac troponin I (cTnI) (green) and desmin (red) counterstained with the nuclear marker 4',6-diamidino-2-phenylindole (DAPI; blue). Desmin was rarely present in grafted cells at 4 weeks (white arrowhead). At 12 weeks, desmin was present in nearly all grafted cells, often displaying a striated pattern similar to cTnI (white arrows). (A1, B1) Higher magnification image of area demarcated by white squares in (A, B). Scale bar: (A, B) 1,000  $\mu$ m, (A1, B1) 100  $\mu$ m.

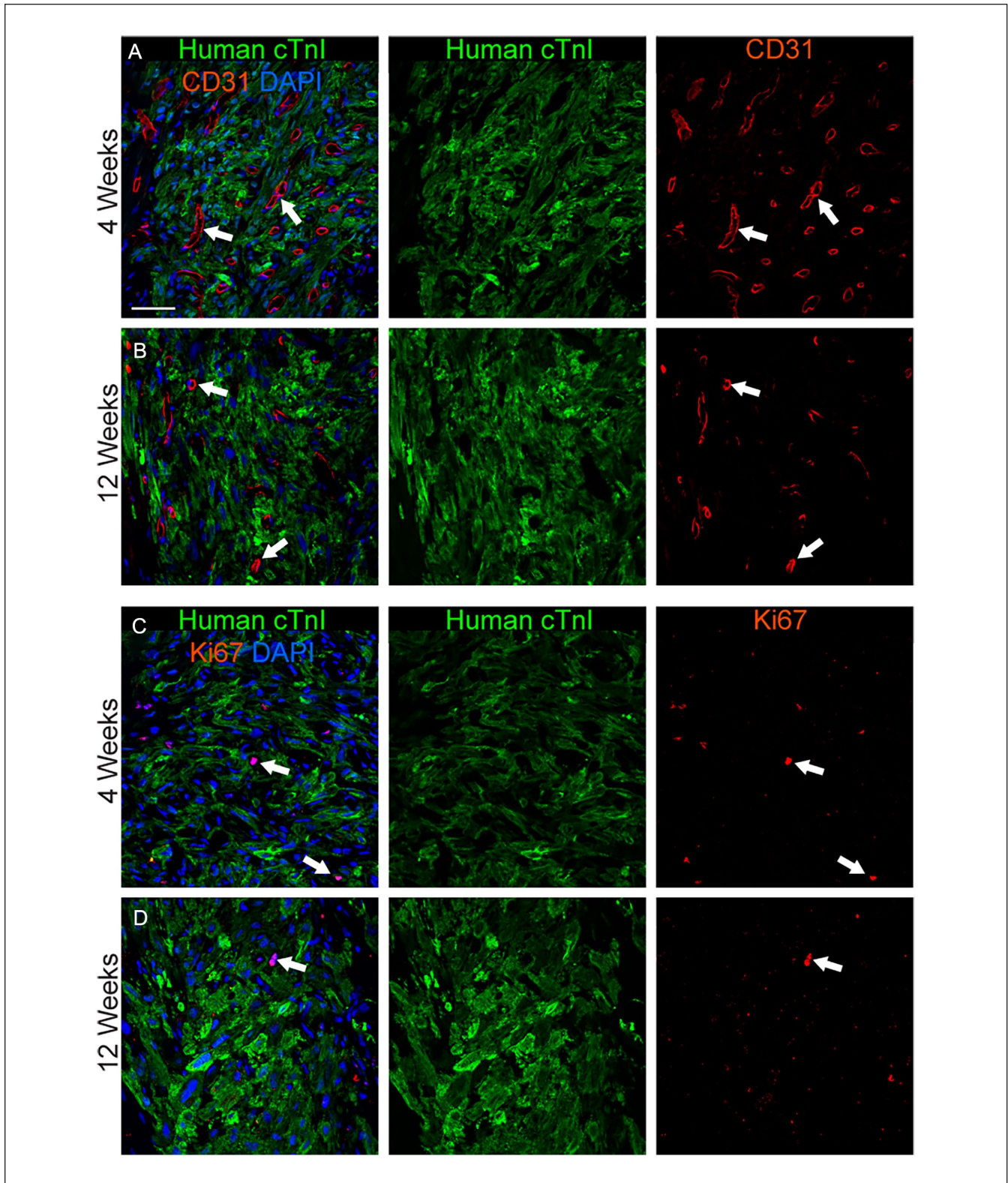


**Figure 6.** Cardiac grafts have similar vascularization and presence of dividing cells at 4 and 12 weeks post-cell delivery. (A–D) Representative images from high-dose 4-week (A, HD4-1; C, HD4-4) and high-dose 12-week (B, HD12-4; d, HD12-1) subjects showing immunofluorescence labeling of human cardiac troponin I (cTnI) (green) and either the endothelial marker CD31 (A, B = red; white arrows) or the dividing cell marker Ki67 (C, D = red; white arrows). Tissue was counterstained with the nuclear marker 4',6-diamidino-2-phenylindole (DAPI; blue). Scale bar: 100  $\mu$ m.

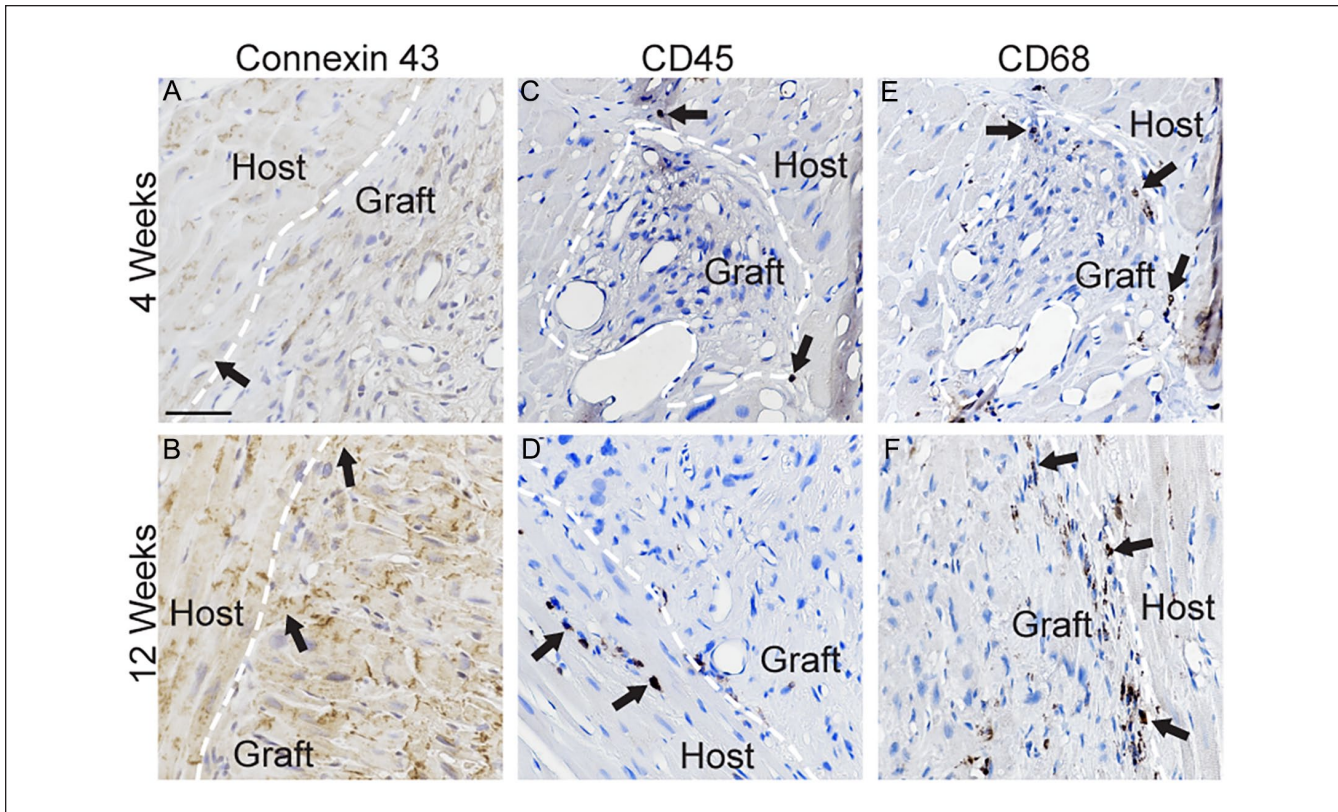


**Figure 7.** Expression of connexin 43 and minimal immune cell labeling in cardiac grafts. (A–F) Representative images from high-dose 4-week (A, C, E, HD4-4) and 12-week (B, HD12-1; D, F, HD12-4) subjects showing immunolabeling for the gap junction marker connexin 43 (A, B = brown; black arrows), immune cell marker CD45 (C, D = brown; black arrows), and macrophage marker CD68 (E, F = brown; black arrows). Tissue was counterstained with hematoxylin (blue). White dashed line is drawn at border of grafted cells. Scale bar: 100  $\mu$ m.

The infiltrates were confirmed to be CD45+ (Fig. 6C, D; Supplementary Fig. 13a, c) or CD68+ (Fig. 6E, F; Supplementary Fig. 13b, d). Remarkably, the three low-dose subjects (LD4-4, LD12-1, and LD12-3) without evidence of grafts also had minimal infiltrates of immune cells. The most intense immune response around a graft area was observed in a low-dose 12-week animal (LD12-4) (Supplementary Fig. 13e, f).

## Discussion

The successful myocardial engraftment of hiPSC-CLs in immunosuppressed rhesus with right ventricular pressure overload indicates the feasibility and safety of the approach for clinical translation. Our strategy is aimed toward treating patients suffering from congenital heart defects involving right ventricular pressure overload. The experiments in this report were designed to inform the clinical translation. For example, the study endpoints were chosen to provide insight on the short-term (4 weeks) and relative long-term (12 weeks) survival, integration, and safety of the cells after intramyocardial injection. These timepoints were within a

standard range utilized in the field of cardiac transplantation for the preclinical evaluation of cell therapies in pigs and monkeys. Patients with single-ventricle cardiac defects undergo a series of necessary palliative surgeries resulting in circulation whereby blood flows passively through the lungs and the right heart pumps to the systemic circulation. Since the right heart is not adequately structured to pump against systemic pressures, a state of ventricular pressure overload occurs that can lead to cardiac failure. We envision hiPSC-CL therapy as an autologous adjunctive treatment to be delivered during the surgical intervention, with the injected cells readily engrafting after administration to provide muscular support to the compromised heart tissue. This cell-based approach is part of our team's investigations toward developing comprehensive solutions for patients with congenital cardiac defects.

PAB to induce right ventricular pressure overload has been previously tested in pigs, mice, dogs, and sheep, but not in monkeys<sup>30</sup>. Our choice of model species was based on the similarity of the cardiovascular and immune systems of macaques and humans<sup>31</sup>, which is critical for preclinical testing of cell-based therapies for cardiac disease. As NHP

models of right ventricular pressure overload were not available, and monkeys born with congenital cardiac defects are rare<sup>32–35</sup>, we adapted the PAB approach to rhesus, based on our previous work in pigs<sup>24</sup>. The translation required careful adjustments to ensure a functional condition. A critical difference between the swine model and our NHP model was the age of the subjects at the time of the procedure, as the pigs were significantly younger (juveniles, 3–4 weeks old) than the monkeys (adults, 4–9 years old). The cardiovascular system of juveniles is quite resilient and resistant to the effects of increased pressure loads as compared to adults. In the juvenile swine PAB model, the animals were pre-loaded with a large bolus of IV fluids, and the PAB was tightened to target almost a doubling of right ventricular pressures and a significant drop (~40%) of systemic pressure, which would be intolerable to an older animal. Specifically, in the juvenile swine model, the systolic mean Doppler gradient average across the PA was  $48 \pm 12$  mmHg, yet the first two monkeys to receive PAB died 3 days later due to acute cardiac insufficiency, while their systolic mean Doppler gradients were only 29 and 27 mmHg, respectively; with the exception of P1 and P2, no NHP received a fluid bolus before PAB placement. Based on these findings, the procedure was further modified to include intraoperative echocardiography to monitor PAB gradient and severity of tricuspid regurgitation during banding. The band tightness was adjusted until reaching a target systolic mean Doppler pressure gradient of 15 to 23 mmHg and mild to moderate tricuspid regurgitation was observed. The monitoring drastically improved survivability and resulted in similar levels of myocardial fibrosis and myofibrillar disarray across subjects.

Blood biomarkers of potential cardiac injury did not detect significant differences between treatment groups, suggesting similarity of the lesions across the enrolled animals and safe grafting procedures. The small group size or the low sensitivity of the test to identify cardiac disease in macaques<sup>36</sup> may have affected the results. Yet, circulating levels of troponin per individual were also not indicative of severe cardiac damage, which matches postmortem histologic findings of myocardial fibrosis and disarray without necrosis. In that regard, although there is an overall paucity of data regarding the histopathology of patients with functional right ventricular pressure overload, the two primary histological features that have been described are fibrosis and myocardial disarray<sup>37</sup>. All the rhesus in this study consistently demonstrated elevated right ventricle pressure and varying degrees of cardiac pathology, with primary features including fibrosis and myocardial disarray, therefore successfully modeling the functional cardiac pressure overload condition.

The intramyocardial cell grafts did not induce significant changes in right (or left) ventricular size or function as measured by echocardiography. For the purposes of this study, it was essential to create a condition where animals would survive the 12-week study duration without cardiac

decompensation. It is possible that refining the model to induce a more severe condition of right ventricular pressure overload, or performing the PAB surgery at a younger age when a higher degree of constriction could be better tolerated, would allow for better detection of efficacy of hiPSC-CL grafts. Alternatively, a longer-duration study could elucidate whether the cell therapy has a beneficial effect in a state of chronic pressure overload. It is also possible that higher cell doses may also be required to improve cardiac function. The doses chosen in this study matched the intended cell dose for humans (2 million cells/kg) with a higher (10 million cells/kg) dose selected for safety reasons. We adapted the cell dosings proposed to treat cardiac ischemia to our envisioned adjunctive treatment of congenital heart disease; our dosings were lower than the ones used in NHP models of cardiac ischemia (e.g.,  $7.5 \times 10^8$ )<sup>10</sup>. Unlike in ischemia, patients with congenital heart disease do not suffer from an acute loss of a large number of cells; thus, a low dose of hiPSC-CLs could potentially be therapeutic while minimizing safety concerns. As these patients often require multiple surgeries, additional cell deliveries could be performed for which a lower (and potentially safer) dose may be more amenable (and well tolerated for autologous grafts). Determining an optimal cell dose will be a critical area of future study, since it is currently unknown what percentage of engraftment would translate to a clinical benefit. A target cell dose for ischemic disease could be calculated based on the size of the lesion, yet the pathology and distribution in congenital heart disease does not lend itself to such estimation. Future studies are warranted to explore model refinement for efficacy evaluation and dose optimization, including dose-escalating efficacy studies for determining cell doses that result in functional benefit.

Although a variety of arrhythmia events occurred in animals receiving hiPSC-CLs and vehicle, VT has previously been described following the administration of SC-derived cardiomyocytes in NHP hearts<sup>8–12</sup>. Out of 16 grafted animals, two experienced incessant VT (sustained VT lasting hours) with one subject succumbing to the arrhythmia 3 days post-surgery, while the second was successfully treated with amiodarone and subsequently completed the 12-week study. All NHPs used in this study were screened for cardiac pathologies and underwent PAB using similar methods developed during the first phase of this study, precluding the role of predisposing, study-related factors that could increase an individual's vulnerability to develop VTs. The cardiac arrhythmias in the rest of our grafted animals were transitory, with VT events detected between 9 and 19 days after cell delivery. Compared to previous reports on SC-derived cardiac grafts in post-ischemic large animals, our study with a non-ischemic cohort exhibited fewer incidents of incessant VT. For example, Chong et al.<sup>8</sup> reported that all six macaques receiving hESC-derived cardiomyocytes experienced incessant VT more than 2 weeks in duration. Liu et al.<sup>10</sup> identified

one case with sustained VT (10 days, constant) after grafting of human ESC-derived cardiomyocytes, although nearly all the monkeys (nine out of 10) had multiple episodes of sustained VT before and following administration of vehicle or treatment. The authors proposed that these arrhythmias were related to the large infarct size sustained following prolonged coronary arterial occlusion. A similar study by Shiba et al.,<sup>38</sup> employing allogenic iPSC-derived cardiomyocytes, detected sustained VT in all five cell-injected macaques. Interestingly, sustained VT was detected in two subjects prior to cell injection, but in none of the five vehicle-treated monkeys<sup>38</sup>. Moreover, pig studies conducted by Romagnuolo and colleagues recorded incidents of incessant VT in all six animals receiving cells, of which three displayed incessant VT for  $\geq 20$  h per day for over 20 days<sup>39</sup>.

Several critical differences between the studies referenced above and this report may explain the substantially shorter duration of VT. All four of the above-mentioned studies involved inducing an arterial blockage to generate ischemia. Remodeling of ischemia-induced fibrotic tissue results in islands of SC-derived cardiomyocytes cut off from functional host cardiomyocytes. In contrast, we delivered hiPSC-CLs across the relatively healthy myocardium of the right ventricle, placing them in direct contact with host cardiomyocytes. Hypothetically, the immediate interaction with synchronized cardiomyocytes should decrease the time required for the hiPSC-CLs to form gap junctions with host cardiomyocytes, limiting the incidence of cardiac arrhythmias. The number of grafted cells per site may also contribute to the onset of VT. Liu et al. transplanted a larger number of cells ( $7.5 \times 10^8$ ) compared to our study (low-dose mean:  $1.4 \times 10^7$ ; high-dose mean:  $7 \times 10^7$ ) in an effort to repair large infarcts affecting substantial areas of the left ventricle. In our study, the total human cTnI+ grafted area relative to the right ventricle area ranged from 0.08% to 2.51%, with an average of approximately 1.5% in the high-dose, 12-week group. This graft size as a percentage of the right ventricle is smaller than, though comparable to, the 1.1%–3.4% range reported by Liu et al.<sup>10</sup>. Notably, the animal in the high-dose group (HD12-1) that had the largest total graft area did not develop VT. This animal was incidentally diagnosed by ultrasound with hypertrophic cardiomyopathy, a condition previously reported in rhesus macaque populations<sup>40</sup>, which may have generated a microenvironment suitable for graft survival. It should be noted that Kobayashi et al.<sup>13</sup> reported less incidence of graft-related arrhythmias after injecting hiPSC-derived cardiac spheroids in a cardiac ischemic macaque model. Interestingly, the cell dosing in their report was within the range of our study (low dose  $2 \times 10^7$ ; high dose:  $6 \times 10^7$ ). Although we identified a significant relationship between graft size and cell dose, the presence of VT events did not correlate with graft size, number of injections, immune response, or PAB-induced pathology. As a solution to graft-induced VTs, Marchiano et al.<sup>41</sup> developed human ESC-derived cardiomyocytes that were genetically modified

to abolish the expression of the depolarization-related genes HCN4, CACNA1H, and SLC8A1, and to overexpress the hyperpolarization-associated gene KCNJ2. When the edited cells were injected into uninjured pig hearts, the animals did not develop VTs. In the clinical setting, it may be prudent to administer antiarrhythmic pharmacotherapy during the period of cell integration into the myocardium.

As per our intended clinical application, we did not employ post-differentiation selection and/or sorting techniques to enrich the percentage of cardiomyocytes; thus, the product is referred to as cardiac lineage cells (i.e., hiPSC-CLs). Although cTnT/cTnI levels varied significantly between the four lots, no differences in engraftment were detected. Cells from lots 2 and 3 (same donor) were used for the three low-dose subjects without detectable grafts, yet the same cells successfully engrafted in other subjects. The electrophysiological profile of the hiPSC-CLs was evaluated with ArcLight, an optical sensor widely used for screening large numbers of cells. The cells were a mixture of atrial and ventricular, with some variability in action potentials across lots. ArcLight methods may have contributed to the variability, as it has a slower frequency response and longer APD90 reported values than patch clamp<sup>19,42,43</sup>. Although no relationship was found between cell lot and cardiac events in grafted subjects, it may be possible that a mismatch between electrophysiological subtypes of the grafted cells and host cardiac chamber facilitated the transient arrhythmias. Interestingly, when Ichimura and colleagues<sup>44</sup> grafted hESC-derived nodal-like and atrial cardiomyocytes into the left ventricle of athymic rats, 12 weeks later, only a ventricular subtype was detected. The authors proposed that, as the atrial cells had lower reproduction rates, they were eventually replaced by the ventricular type, which could explain the transient nature of the arrhythmias in their rat study and other reported experiments using large animal models, including ours<sup>10,38,39</sup>. Another possibility is that the ventricular host cells provide environmental cues to minimize proliferation of atrial type cells and/or induce a ventricular-like phenotype of the engrafted cardiomyocytes over time.

It is currently unclear why three animals in the low-dose group did not have detectable human cTnI+ grafts. The smaller starting number of cells relative to the high-dose group may have simply limited the number of available cells for survival; however, in other subjects, a similar number of injected cells produced visible grafts. Low cell viability is unlikely because cells were frozen in lots and engraftment occurred in all lots (viability after suspension in freezing media was 98%–99%). In addition, the same skilled surgeon performed the intramyocardial cell injections using the same methods and tools for all animals. Host rejection of the xenografts may have occurred, despite the intense immunosuppression based on a previously reported regimen<sup>10</sup> that was modified and validated in the pilot phase of this study. Therapeutic levels of tacrolimus were maintained in all animals throughout the course of the study. Following standard



clinical procedures, we did not measure the levels of methylprednisolone and abatacept; therefore, we cannot rule out sub-therapeutic levels of these drugs. However, the size, integration, and organization of the grafts appeared to be unaffected by the host immune system, and a minimal immune response was observed, including in the three low-dose animals without detectable grafts. It is possible that, at the time of the tissue collection (4–12 weeks after cell delivery), any elicited immune response had resolved, and immune cells were no longer present. Studies with additional, earlier timepoints may shed light on the immune response to cardiomyocytes grafted into a model of right ventricular pressure overload. Clinical translation of this approach will benefit from the use of autologous sources for hiPSC generation, which, albeit more laborious, decreases rejection risk and eliminates the requirement of immunosuppression. In that regard, our use of different cell lots obtained from several donors supports the feasibility of generating multiple cell lines from autologous sources.

The hiPSC-CL grafts displayed increased integration, maturity, and organization over time. At 4 weeks post grafting (at the time arrhythmic events subsided), we observed minimal alignment of human cardiomyocytes in the periphery of the graft with surrounding host cells. By 12 weeks, grafted areas displayed a mature morphology and organization at the core of the graft site that matched the host myocardium. Furthermore, at 12 weeks, the grafted human cells robustly expressed desmin, an intermediate filament protein integral to the cardiomyocyte cytoskeletal network, which increases expression with cardiomyocyte maturity<sup>45</sup>. Overall, few mitotic profiles were observed; further identification of Ki67+ dividing cell types was not performed, as available human-specific nuclear protein markers cross react with rhesus tissue. Cardiomyocytes are terminally differentiated cells that do not proliferate at any significant rate. The spontaneously beating immature hiPSC-derived cardiomyocytes used in this study only exhibit about a 5% EdU incorporation rate in vitro (unpublished data, Nelson lab), thus indicating that very few cells are entering S-phase of the cell cycle at any given time. Genetic manipulation of hiPSCs used in cardiomyocyte differentiation assays, for example, knocking out cell cycle control genes, could increase the proliferation rate of the engrafted cells, yet it is not recommended due to the risk of generating tumors. Alternatively, techniques for improved engraftment that could also stimulate cell proliferation, like co-transplantation with extracellular matrix proteins (e.g., Matrigel) or overexpression of connective tissue growth factors, are being investigated<sup>46</sup>. It should be noted that cardiomyocyte turnover is less than 1% in the adult human heart<sup>47</sup>, suggesting that cardiomyocytes function for many years before being replaced under normal conditions, a capacity expected from grafted cardiomyocytes. The periphery of the grafts showed an increase in interdigitation between human cTnI+ and host cardiomyocytes between 4 and 12 weeks, which matched the minimal fibrosis observed

at 4 weeks that resolved by 12 weeks. The observed fibrosis is consistent with needle passage and cell delivery initiating local cardiac repair mechanisms. Cardiac injury activates interstitial myofibroblasts, prompting the secretion and deposition of extracellular matrix proteins, which are critical to wound healing<sup>48</sup>. The expression of connexin 43, a gap junction protein, suggested points of interaction between graft and host cardiomyocytes that were greater at 12 weeks compared to 4 weeks. Future studies would benefit from spatial genomics assays to generate gene expression data at the single-cell level regarding grafted cells' maturation states. Graft versus host cardiomyocyte organization could be evaluated with intelligent programs considering multidirectional vectors across the ROI. These approaches, combined with experiments with additional timepoints and electrophysiological studies, can further characterize the progression in graft cell morphology and integration into the host myocardium over time, as well as the functional, electrical, and molecular interactions between graft and host.

The clinical application of this cell technology is significant for the congenital heart defect community, as all these patients will experience decreased heart function within their lifetime. The results of this study provide key information about product safety and effective delivery which directly will inform clinical trial design. There are several challenges and considerations for scaling up this approach for patients with congenital heart defects. Current manufacturing methods are capable of production for early phase clinical trials. Adoption of closed and semi-automated platforms will be required to scale manufacturing for later phase studies. The development of a potency assay along with early phase in-human data will inform refinement of final product characteristics. Last, as direct access to the heart is a challenge for our target population, investigation of techniques for minimally invasive product administration will play a key role in scale up. Cell delivery via catheter would allow for scheduled, lower risk intervention, capable of aligning with the manufacture of patient-specific cell products.

Overall, our results in a novel NHP model establish the feasibility and safety of this strategy as an adjunctive treatment for ventricular pressure overload and support the advancement of this treatment into clinical trials for patients with severe and untreatable heart failure due to non-ischemic congenital heart defects.

### Acknowledgments

Cell products were produced under a co-development agreement with HeartWorks, Rochester, MN, 55905. Implantable Cardiac Monitor devices were generously donated by Medtronic. This work was made possible due to the dedication and expertise of the technical, pathology, and veterinary staff at the Wisconsin National Primate Research Center, especially A. Moy, K. Fuchs, R. Putney, T. Roehling, K. Lafferty, M. Berg, and L. Wierenga. We are grateful to C. Reece, A. Breuer, and A. Possell for performing cardiac

ultrasounds and to J. Pedersen, S. Edgerton, D. Seisler, T. Weston, G. Theobald, and M. Hall for study support.

### Author Contributions

J.S., F.S., T.N., and M.E.E. conceived the research. J.S., F.S., T.N., J.K., J.M.M., H.A.S., and M.E.E. supervised the research. F.S., M.C., and N.F. conducted cell experiments. J.S., J.K., J.C., J.W., Y.Q., S.C., and F.C. performed *in vivo* experimental work. A.Z., D.V., S.J.J., H.A.S., P.B., A.M., J.M.H., V.B., and J.M.M. performed post-mortem experimental work. J.S., F.S., R.R., C.H., F.C., J.M.M., and M.E.E. performed analysis. All authors participated in data interpretation. J.S., F.S., J.M.M., and M.E.E. wrote the manuscript with input from all authors. All authors read and approved the final manuscript.

### Data Availability

All requests for raw and analyzed data and materials will be promptly reviewed by the corresponding authors, the Mayo Clinic, and the University of Wisconsin-Madison to verify whether the request is subject to any intellectual property or confidentiality obligations. Any data and materials that can be shared will be released via a Material Transfer Agreement. The RNAseq data generated in this study have been deposited in the GEO database under accession code GSE234206.

### Ethical Approval

The present study was performed in strict accordance with the US Animal Welfare Act and regulations and recommendations in the National Research Council Guide for the Care and Use of Laboratory Animals (8th edition, 2011) in an AAALAC accredited facility (Wisconsin National Primate Research Center (WNPRC), University of Wisconsin-Madison) with the approval of the IACUC. All efforts were made to minimize the number of animals utilized and to ameliorate any distress. Human dermal punch biopsies were obtained following documented review and approval from the Institutional Review Board (IRB # 10-006845) at Mayo Clinic, Rochester, MN, USA, and collected following written informed consent by the patient, in accordance with the Declaration of Helsinki.

### Statement of Human and Animal Rights

This article does not contain any studies with human subjects. Statements pertaining to the use of animal subjects in this article can be found in the 'Ethical Approval' section.

### Statement of Informed Consent

There are no human subjects in this article and informed consent is not applicable.

### Declaration of Conflicting Interests

The author(s) declared no potential conflicts of interest with respect to the research, authorship, and/or publication of this article.

### Funding

The author(s) disclosed receipt of the following financial support for the research, authorship, and/or publication of this article: This research was supported by the Todd and Karen Wanek Family Program for HLHS. We also acknowledge the support of the NIH award P51OD011106.

### ORCID iDs

Yasir Qureshi  <https://orcid.org/0000-0002-9898-2318>

Marina E. Emborg  <https://orcid.org/0000-0002-9351-6641>

### Supplemental Material

Supplemental material for this article is available online.

### References

- Garcia AM, Beatty JT, Nakano SJ. Heart failure in single right ventricle congenital heart disease: physiological and molecular considerations. *Am J Physiol Heart Circ Physiol*. 2020;318(4):H947–65.
- Khairy P, Poirier N, Mercier LA. Univentricular heart. *Circulation*. 2007;115(6):800–12.
- Lewis M, Rosenbaum M. The miracle baby grows up: hypoplastic left heart syndrome in the adult. *Curr Cardiol Rep*. 2017;19(8):74.
- Niebler RA, Shah TK, Mitchell ME, Woods RK, Zangwill SD, Tweddell JS, Berger S, Ghanayem NS. Ventricular assist device in single-ventricle heart disease and a superior cavopulmonary anastomosis. *Artif Organs*. 2016;40(2):180–4.
- Chu MWA, Gersch KA, Rodriguez E, Nifong LW, Chitwood WR. Robotic "haircut" mitral valve repair: posterior leaflet-plasty. *Ann Thorac Surg*. 2008;85(4):1460–62.
- Bleiweis MS, Fudge JC, Peek GJ, Vyas HV, Cruz Beltran S, Pitkin AD, Sullivan KJ, Hernandez-Rivera JF, Philip J, Jacobs JP. Ventricular assist device support in neonates and infants with a failing functionally univentricular circulation. *JTCVS Tech*. 2022;13:194–204.
- Greenberg JW, Raees MA, Dani A, Heydarian HC, Chin C, Zafar F, Lehenbauer DG, Morales DLS. Palliated hypoplastic left heart syndrome patients experience superior waitlist and comparable post-heart transplant survival to non-single ventricle congenital heart disease patients. *Semin Thorac Cardiovasc Surg*. 2022;36:230–41.
- Chong JJ, Yang X, Don CW, Minami E, Liu YW, Weyers JJ, Mahoney WM, Van Biber B, Cook SM, Palpant NJ, Gantz JA, et al. Human embryonic-stem-cell-derived cardiomyocytes regenerate non-human primate hearts. *Nature*. 2014;510(7504):273–77.
- Kawamura T, Miyagawa S, Fukushima S, Maeda A, Kashiyama N, Kawamura A, Miki K, Okita K, Yoshida Y, Shiina T, Ogasawara K, et al. Cardiomyocytes derived from MHC-homozygous induced pluripotent stem cells exhibit reduced allogeneic immunogenicity in MHC-matched non-human primates. *Stem Cell Rep*. 2016;6(3):312–20.
- Liu Y-W, Chen B, Yang X, Fugate JA, Kalucki FA, Futakuchi-Tsuchida A, Couture L, Vogel KW, Astley CA, Baldessari A, Ogle J, et al. Human embryonic stem cell-derived cardiomyocytes restore function in infarcted hearts of non-human primates. *Nat Biotechnol*. 2018;36(7):597–605.
- Wang X, Han Z, Yu Y, Xu Z, Cai B, Yuan Y. Potential applications of induced pluripotent stem cells for cardiovascular diseases. *Curr Drug Targets*. 2019;20(7):763–74.
- Cheng YC, Hsieh ML, Lin CJ, Chang CMC, Huang CY, Puntney R, Wu Moy A, Ting CY, Herr Chan DZ, Nicholson MW, Lin PJ, et al. Combined treatment of human induced pluripotent stem cell-derived cardiomyocytes and endothelial cells

- regenerate the infarcted heart in mice and non-human primates. *Circulation*. 2023;148(18):1395–409.
13. Kobayashi H, Tohyama S, Ichimura H, Ohashi N, Chino S, Soma Y, Tani H, Tanaka Y, Yang X, Shiba N, Kadota S, et al. Regeneration of nonhuman primate hearts with human induced pluripotent stem cell-derived cardiac spheroids. *Circulation*. 2024;150:611–21.
  14. Menasché P, Vanneaux V, Hagège A, Bel A, Cholley B, Parouchev A, Cacciapuoti I, Al-Daccak R, Benhamouda N, Blons H, Agbulut O, et al. Transplantation of human embryonic stem cell-derived cardiovascular progenitors for severe ischemic left ventricular dysfunction. *J Am Coll Cardiol*. 2018;71(4):429–38.
  15. Yap L, Chong LY, Tan C, Adusumalli S, Seow M, Guo J, Cai Z, Loo SJ, Lim E, Tan RS, Grishina E, et al. Pluripotent stem cell-derived committed cardiac progenitors remuscularize damaged ischemic hearts and improve their function in pigs. *NPJ Regen Med*. 2023;8(1):26.
  16. Navaratnarajah CK, Pease DR, Halfmann PJ, Taye B, Barkhymer A, Howell KG, Charlesworth JE, Christensen TA, Kawaoka Y, Cattaneo R, Schneider JW, et al. Highly efficient SARS-CoV-2 infection of human cardiomyocytes: spike protein-mediated cell fusion and its inhibition. *J Virol*. 2021;95(24):e0136821.
  17. Secreto FJ, Li X, Smith AJ, Bruinsma ES, Perales-Clemente E, Oommen S, Hawse G, Hrstka SCL, Arendt BK, Brandt EB, Wigle D, et al. Quantification of etoposide hypersensitivity: a sensitive, functional method for assessing pluripotent stem cell quality. *Stem Cells Transl Med*. 2017;6(10):1829–39.
  18. Chen VC, Ye J, Shukla P, Hua G, Chen D, Lin Z, Liu JC, Chai J, Gold J, Wu J, Hsu D, et al. Development of a scalable suspension culture for cardiac differentiation from human pluripotent stem cells. *Stem Cell Res*. 2015;15(2):365–75.
  19. Biendarra-Tiegs SM, Li X, Ye D, Brandt EB, Ackerman MJ, Nelson TJ. Single-cell RNA-sequencing and optical Electrophysiology of human induced pluripotent stem cell-derived cardiomyocytes reveal discordance between cardiac subtype-associated gene expression patterns and electrophysiological phenotypes. *Stem Cells Dev*. 2019;28(10):659–73.
  20. Kalari KR, Nair AA, Bhavsar JD, O'Brien DR, Davila JJ, Bockol MA, Nie J, Tang X, Baheti S, Doughty JB, Middha S, et al. MAP-RSeq: mayo analysis pipeline for RNA sequencing. *BMC Bioinform*. 2014;15(1):224.
  21. Liao Y, Smyth GK, Shi W. The Subread aligner: fast, accurate and scalable read mapping by seed-and-vote. *Nucleic Acids Res*. 2013;41(10):e108.
  22. Dobin A, Davis CA, Schlesinger F, Drenkow J, Zaleski C, Jha S, Batut P, Chaisson M, Gingeras TR. STAR: ultrafast universal RNA-seq aligner. *Bioinformatics*. 2012;29(1):15–21.
  23. Robinson MD, McCarthy DJ, Smyth GK. edgeR: a bioconductor package for differential expression analysis of digital gene expression data. *Bioinformatics*. 2010;26(1):139–40.
  24. Oommen S, Cantero Peral S, Qureshi MY, Holst KA, Burkhart HM, Hathcock MA, Kremers WK, Brandt EB, Larsen BT, Dearani JA, Edwards BS, et al. Autologous umbilical cord blood-derived mononuclear cell therapy promotes cardiac proliferation and adaptation in a porcine model of right ventricle pressure overload. *Cell Transplant*. 2022;31:9636897221120434.
  25. Cantero Peral S, Burkhart HM, Oommen S, Yamada S, Nyberg SL, Li X, O'Leary PW, Terzic A, Cannon BC, Nelson TJ. Safety and feasibility for pediatric cardiac regeneration using epicardial delivery of autologous umbilical cord blood-derived mononuclear cells established in a porcine model system. *Stem Cells Transl Med*. 2015;4(2):195–206.
  26. Metzger JM, Matsoff HN, Zinnen AD, Fleddermann RA, Bondarenko V, Simmons HA, Mejia A, Moore CF, Emborg ME. Post mortem evaluation of inflammation, oxidative stress, and PPARgamma activation in a nonhuman primate model of cardiac sympathetic neurodegeneration. *PLoS ONE*. 2020;15(1):e0226999.
  27. Metzger JM, Moore CF, Boettcher CA, Brunner KG, Fleddermann RA, Matsoff HN, Resnikoff HA, Bondarenko V, Kamp TJ, Hacker TA, Barnhart T, et al. In vivo imaging of inflammation and oxidative stress in a nonhuman primate model of cardiac sympathetic neurodegeneration. *NPJ Parkinsons Dis*. 2018;4:22.
  28. Joers V, Dilley K, Rahman S, Jones C, Shultz J, Simmons H, Emborg ME. Cardiac sympathetic denervation in 6-OHDA-treated nonhuman primates. *PLoS ONE*. 2014;9(8):e104850.
  29. Blin G, Nury D, Stefanovic S, Neri T, Guillevic O, Brinon B, Bellamy V, Rücker-Martin C, Barbry P, Bel A, Bruneval P, et al. A purified population of multipotent cardiovascular progenitors derived from primate pluripotent stem cells engrafts in postmyocardial infarcted nonhuman primates. *J Clin Invest*. 2010;120(4):1125–39.
  30. Andersen A, van der Feen DE, Andersen S, Schultz JG, Hansmann G, Bogaard HJ. Animal models of right heart failure. *Cardiovasc Diagn Ther*. 2020;10(5):1561–79.
  31. Cox LA, Olivier M, Spradling-Reeves K, Karere GM, Comuzzie AG, VandeBerg JL. Nonhuman primates and translational research-cardiovascular disease. *Ilar J*. 2017;58(2):235–50.
  32. Brandt DJ, Canfield DR, Peterson PE, Hendrickx AG. Persistent truncus arteriosus in a rhesus monkey (*Macaca mulatta*). *Comp Med*. 2002;52(3):269–72.
  33. Jerome CP. Congenital malformations and twinning in a breeding colony of Old World Monkeys. *Lab Anim Sci*. 1987;37(5):624–30.
  34. Swindle MM, Kan JS, Adams RJ, Starr FL III, Samphilipo MA Jr, Porter WP. Ventricular septal defect in a rhesus monkey. *Lab Anim Sci*. 1986;36(6):693–95.
  35. Liu DX, Gilbert MH, Kempf DJ, Didier PJ. Double-outlet right ventricle and double septal defects in a Rhesus macaque (*Macaca mulatta*). *J Vet Diagn Invest*. 2012;24(1):188–91.
  36. Ueda Y, Yee JL, Williams A, Roberts JA, Christie KL, Stern JA. Identifying cardiac diseases using cardiac biomarkers in rhesus macaques (*Macaca mulatta*). *Comp Med*. 2020;70(5):348–57.
  37. Files MD, Arya B. Pathophysiology, adaptation, and imaging of the right ventricle in Fontan circulation. *Am J Physiol Heart Circ Physiol*. 2018;315(6):H1779–88.
  38. Shiba Y, Gomibuchi T, Seto T, Wada Y, Ichimura H, Tanaka Y, Ogasawara T, Okada K, Shiba N, Sakamoto K, Ido D, et al. Allogeneic transplantation of iPSC cell-derived cardiomyocytes regenerates primate hearts. *Nature*. 2016;538(7625):388–91.
  39. Romagnuolo R, Masoudpour H, Porta-Sánchez A, Qiang B, Barry J, Laskary A, Qi X, Massé S, Magtibay K, Kawajiri H, Wu J, et al. Human embryonic stem cell-derived cardiomyocytes regenerate the infarcted pig heart but induce ventricular tachyarrhythmias. *Stem Cell Rep*. 2019;12(5):967–81.
  40. Reader JR, Canfield DR, Lane JF, Kanthaswamy S, Ardeshir A, Allen AM, Tarara RP. Left ventricular hypertrophy in rhesus

- macaques (*Macaca mulatta*) at the California National Primate Research Center (1992-2014). *Comp Med*. 2016;66(2):162–69.
41. Marchiano S, Nakamura K, Reinecke H, Neidig L, Lai M, Kadota S, Perbellini F, Yang X, Klaiman JM, Blakely LP, Karbassi E, et al. Gene editing to prevent ventricular arrhythmias associated with cardiomyocyte cell therapy. *Cell Stem Cell*. 2023;30(4):396–414.e9.
  42. Leyton-Mange JS, Mills RW, Macri VS, Jang MY, Butte FN, Ellinor PT, Milan DJ. Rapid cellular phenotyping of human pluripotent stem cell-derived cardiomyocytes using a genetically encoded fluorescent voltage sensor. *Stem Cell Rep*. 2014;2(2):163–70.
  43. Lee S, Geiller T, Jung A, Nakajima R, Song YK, Baker BJ. Improving a genetically encoded voltage indicator by modifying the cytoplasmic charge composition. *Sci Rep*. 2017;7(1):8286.
  44. Ichimura H, Kadota S, Kashihara T, Yamada M, Ito K, Kobayashi H, Tanaka Y, Shiba N, Chuma S, Tohyama S, Seto T, et al. Increased predominance of the matured ventricular subtype in embryonic stem cell-derived cardiomyocytes in vivo. *Sci Rep*. 2020;10(1):11883.
  45. Kim HD. Expression of intermediate filament desmin and vimentin in the human fetal heart. *Anat Rec*. 1996;246(2):271–78.
  46. Zhu W, Zhao M, Mattapally S, Chen S, Zhang J. CCND2 overexpression enhances the regenerative potency of human induced pluripotent stem cell-derived cardiomyocytes: remuscularization of injured ventricle. *Circ Res*. 2018;122(1):88–96.
  47. Bergmann O, Zdunek S, Felker A, Salehpour M, Alkass K, Bernard S, Sjöstrom SL, Szewczykowska M, Jackowska T, Dos Remedios C, Malm T, et al. Dynamics of cell generation and turnover in the human heart. *Cell*. 2015;161(7):1566–75.
  48. Frangogiannis NG. Cardiac fibrosis. *Cardiovasc Res*. 2021;117(6):1450–88.